The Impact of Assimilation of GPM Microwave Imager Clear-Sky Radiance on Numerical Simulations of Hurricanes Joaquin (2015) and Matthew (2016) with the HWRF model

Zhaoxia Pu and Chaulam Yu

Department of Atmospheric Sciences, University of Utah, Salt Lake City, Utah

Vijay Tallapragada

Environmental Modeling Center, NCEP/NOAA, College Park, Maryland

Jianjun Jin

Goddard Earth Sciences Technology and Research, Universities Space Research Center,

Columbia, Maryland

Will McCarty

Global Modeling and Assimilation Office, NASA Goddard Space Flight Center,

*Greenbelt, M*aryland

Corresponding Author Address: Dr. Zhaoxia Pu, Department of Atmospheric Sciences,

University of Utah, 135 S 1460 E, Rm. 819, Salt Lake City, UT 84112

E-mail: Zhaoxia.Pu@utah.edu

Abstract

The impact of assimilating Global Precipitation Mission (GPM) Microwave Imager (GMI) clear-sky radiance on the track and intensity forecasts of two Atlantic hurricanes during the 2015 and 2016 hurricane seasons is assessed using the Hurricane Weather Research and Forecasting (HWRF) model. The GMI clear-sky brightness temperature is assimilated using a Gridpoint Statistical Interpolation (GSI)-based hybrid ensemble-variational data assimilation system, which utilizes the Community Radiative Transfer Model (CRTM) as a forward operator for satellite sensors. A two-step bias correction approach, which combines a linear regression procedure and variational bias correction, is used to remove most of the systematic biases prior to data assimilation.

Forecast results show that assimilating GMI clear-sky radiance has positive impacts on both track and intensity forecasts, with the extent depending on the phase of hurricane evolution. Forecast verifications against dropsonde soundings and reanalysis data show that assimilating GMI clear-sky radiance, when it does not overlap with overpasses of other microwave sounders, can improve forecasts of both thermodynamic (e.g., temperature and specific humidity) and dynamic variables (geopotential height and wind field), which in turn lead to better track forecasts and a more realistic hurricane inner-core structure. Even when other microwave sounders are present (e.g., AMSU-A, ATMS, MHS, etc.), the assimilation of GMI still reduces temperature forecast errors in the near-hurricane environment, which has a significant impact on the intensity forecast.

1. Introduction

Since the 1990s, satellite observations have become a major source of observations for numerical weather prediction (NWP), owing to the rapid development of radiative transfer models, data assimilation technologies, and launches of numerous major satellites. Specifically, data assimilation allows the incorporation of observational information into the NWP system if the transformation of analysis variables into the form of observations is achievable. For satellite radiance observations, this can be accomplished by using fast radiative transfer models, which simulate the satellite-observed radiances for a given atmospheric state, satellite scan geometry, and surface properties. The atmospheric state is then adjusted according to differences between simulated and observed radiances such that the final analysis is at the maximum likelihood (e.g., Derber and Wu 1998). Many studies have demonstrated the added benefits to NWP of directly assimilating satellite radiance observations in both global models (Derber and Wu 1998; McNally et al. 2000; Okamoto and Derber 2006; Bauer et al. 2006; Miyoshi and Sato 2007; Sakamoto and Christy 2009; Goerss 2009; Aravéquia et al. 2011; Hoppel et al. 2013) and regional models (e.g., Zou et al. 2011; Liu et al. 2012; Qin et al. 2013; M. Zhang et al. 2013; S. Zhang et al. 2013; Kazumori 2014; Wang wt al. 2015; Lin et al. 2017).

So far, the assimilation of radiance observations are known to be able to significantly reduce error in NWP, specifically over regions where conventional observations are sparse. For instance, hurricane forecasts, in particular, benefit greatly from the large spatial coverage over oceans and the high temporal resolution of satellite observations. This is because hurricanes form and evolve mostly over the oceans, where conventional observations such as radiosonde and surface observations are less available. Since the last decade, the research community has devoted great effort to assimilating satellite observations to improve hurricane track and intensity predictions

67 (Pu et al. 2002 and 2008; Pu and Zhang 2010; Liu et al. 2012; Xu et al. 2013; Zou et al. 2013;

68 Zhang and Pu 2014; Yang et al. 2016; Xu et al. 2016; Wu et al. 2016). Specifically, these previous

69 studies found that satellite microwave sounders is particularly useful for understanding moist

70 processes associated with hurricanes owing to its unique capability to depict precipitation structure

71 and moisture processes.

72   Global Precipitation Measurement (GPM) is a recent constellation-based satellite mission with

73 microwave imagery that was initiated by the National Aeronautics and Space Administration

74 (NASA) and the Japan Aerospace Exploration Agency (JAXA). Building upon the success of its

75 predecessor, the Tropical Rainfall Measuring Mission (TRMM), GPM aims to unify and advance

76 next-generation precipitation measurement from a constellation of both research and operational

77 satellites (Hou et al. 2014). Launched on 28 February 2014, the GPM core observatory is equipped

78 with the first spaceborne dual-frequency precipitation radar, and a conical-scanning multichannel

79 microwave imager. Specifically, the GPM Microwave Imager (GMI) not only inherits the nine

80 channels of the TRMM Microwave Imager (TMI) to detect heavy to light precipitation, but also

81 includes four additional high-frequency channels (166 GHz and 183 GHz) to improve sensitivity

82 to and detection of snowfall. In addition, GMI at least doubles the spatial resolution of the channels

83 in TMI and has one of the highest resolutions among the group of GPM constellation satellites.

84 Furthermore, the outstanding calibration of GMI also serves as a reference for the intercalibration

85 of other microwave sounders in the GPM constellation to ensure a physically consistent brightness

86 temperature.

87   Because of the numerous improvements that GPM brings compared to TRMM, it is expected

88 that assimilating GMI radiance will have a positive impact on hurricane track and intensity

89 forecasts. In this study, we investigate the impact of assimilating GMI clear-sky radiance on

90   hurricane track and intensity forecasts using the National Centers for Environmental Prediction

91   (NCEP) Hurricane Weather Research and Forecasting (HWRF) model and the Gridpoint Statistical

92   Interpolation (GSI)-based hybrid of ensemble and three-dimensional variational (3DVar) data

93   assimilation systems. Two notable Atlantic hurricane cases, Hurricanes Joaquin (2015) and

94   Matthew (2016), are used for case studies in this paper.

95   The paper is organized as follows: Section 2 gives a brief introduction to the GMI

96   observations, HWRF model, GSI data assimilation system, hurricane cases, and experimental

97   setting designs. Section 3 provides details about quality control (QC) and bias correction (BC).

98   Assimilation and forecast results and validation of the data impact are discussed in Section 4.

99   Section 5 summarizes results and provides concluding remarks.

2. GMI observations, HWRF model, data assimilation system, and experimental configurations

102   *a. GMI observations*

103   GMI is a conical scanning passive microwave radiometer with 13 microwave channels,

104   ranging from 10 GHz to 183 GHz. Channels 1 to 9 of GMI have frequencies (10 GHz to 89 GHz)

105   similar to those of its predecessor, the TRMM Microwave Imager (TMI). Responsible for sensing

106   liquid precipitation and the lower-troposphere moisture profile, these channels obtain moisture and

107   temperature information in the lower troposphere (> 800 hPa). In addition, GMI includes four

108   high-frequency channels (Ch. 10 to 13) that are responsible for detection of light precipitation and

109   snowfall. Using a conical scan design, the GMI main reflector has a rotation rate of 32 rpm,

110   scanning a 140° sector centered on the spacecraft ground track with an altitude of about 407 km.

111   This scan configuration gives a cross-track swath covering roughly 885 km above the earth's

112   surface. In terms of scan geometry, GMI uses two sets of scan angles for the thirteen channels.

113 The first nine channels scan at an off-nadir angle of 48.5 °, while the remaining four channels scan

114 at 45.46 ° (see details in Hou et al. 2014). In this study, the GMI Level 1C-R common calibrated

115 and co-registered high-frequency and low-frequency brightness temperature data in all 13

116 microwave channels are assimilated.

117 *b. HWRF model, data assimilation system, and the forward model*

118   The HWRF system was developed at NCEP to provide numerical guidance for the

119 forecasting of tropical cyclone tracks, intensity, and structure (Gopalakrishnan et al. 2011). It uses

120 the Nonhydrostatic Mesoscale Model (NMM) core of the Weather Research and Forecasting

121 (WRF) system as its dynamic solver. Since 2011, HWRF has adopted a triply nested domain

122 configuration. Specifically, HWRF Version 3.7 (see details in Tallapragada et al. 2015) is used in

123 this study, in which the parent domain is configured with 18-km horizontal resolution, covering

124 roughly $80° \times 80°$ on a rotated latitude/longitude E-staggered grid. The intermediate and inner

125 nest domains are two-way interactive nesting and move along with the storm, with resolutions of

126 about 6 km and 2 km, covering about $12° \times 12°$ and $7.1° \times 7.1°$, respectively (see Figure 1). The

127 configuration of the HWRF model is set as close as possible to the operational HWRF model in

128 the hurricane season of 2015.

129   The current data assimilation system for HWRF is the NCEP Gridpoint Statistical

130 Interpolation (GSI)-based hybrid ensemble–three dimensional variational (3DVar) data

131 assimilation system. The cost function used in the data assimilation system is defined as:

132 $$J(x) = \frac{1}{2}(x - x^b)^T (\beta_1 B_1 + \beta_2 B_2)^{-1}(x - x^b) + \frac{1}{2} \left(y_0 - H(x)\right)^T R^{-1}\left(y_0 - H(x)\right) \qquad (1)$$

133

134 where the first term is the background error term with a hybrid background error covariance, which

135 is a sum of two parts: a prescribed static matrix B_1 and a flow-dependent part of the background

136 covariance matrix B_2 estimated using the 6-h forecast of the 80-member ensemble Kalman filter

137 (EnKF) for the NCEP Global Forecast System (GFS). The weighting factors for (β_1 and β_2) are

138 set to be 0.2 and 0.8, respectively. The second term is an observational error term. The operator H

139 is the forward model, which includes the Community Radiative Transfer Model (CRTM) as its

140 radiative transfer component for satellite radiance assimilation. CRTM is a fast-radiative transfer

141 model developed by the Joint Center for Satellite Data Assimilation (JCSDA) at NOAA. A

142 comprehensive description of CRTM can be found in Han et al. (2006) and Weng (2007). CRTM

143 is able to simulate radiances of a large number of sensors onboard, including GMI. For clear-sky

144 simulation over the ocean, basic inputs include atmospheric vertical profiles (e.g., temperature,

145 specific humidity), surface parameters (e.g., surface temperature, wind speed and direction) and

146 sensor geometry (e.g., sensor zenith angle, sensor height). In addition to radiance computation,

147 CRTM also includes calculation of the Jacobian and adjoint model for facilitating various data

148 assimilation–related applications.

149 *c. Experimental configurations*

150   In this study, two notable recent hurricanes cases, Hurricane Joaquin (2015) and Hurricane

151 Matthew (2016), are selected in order to examine the impact of assimilation of GMI clear-sky

152 radiance on hurricane track and intensity forecasts.

153   Before data assimilation, the HWRF model employs a vortex initialization procedure (Liu et

154 al. 2006) to correct the storm position and intensity approach to the real-time estimation (see details

155 in Tallapragada et al. 2015). This procedure consists of two components: a vortex relocation, which

156 places the hurricane vortex at the location from the National Hurricane Center (NHC) tropical

157 cyclone vital statistics (TCVitals) database, and an intensity and size correction, which adjusts the

158 intensity and vortex structure using the TCVitals database. However, previous studies have shown

159 that vortex initialization and data assimilation counteract each other in some cases (Tallapragada

160   et al. 2015). In addition, vortex initialization can also induce imbalances in the initial conditions

161   and lead to vortex spin-down problems in HWRF forecasts in some cases (Pu et al. 2016). In these

162   situations, impacts from data assimilation can be hard to interpret clearly. *In order to clearly*

163   *demonstrate the impact of GMI data assimilation, the intensity correction component is turned off*

164   *in all data assimilation experiments presented in this study.* However, *the vortex relocation is still*

165   *used for data assimilation experiments* to avoid potential phase errors that may put observations

166   in wrong locations and result harm to the vortex inner-core.

167   In addition, the current operational HWRF uses the NCEP Global Forecast System (GFS)

168   analysis to initialize the outer domain (d01) and also uses the GFS forecast to provide the boundary

169   conditions for d01. Since observations over the parent domain are already assimilated in the global

170   data assimilation, the operational HWRF data assimilation is performed only at the inner 6- and 2-

171   km nests (Biswas et al. 2015). However, since GMI radiance has not yet been assimilated in the

172   operational GFS, assimilation of GMI radiance over the parent domain is desired in order to assess

173   its full data impact. To achieve this, we initialize the parent domain using the GFS 6-hour forecast,

174   employing the same procedure as in the inner 6- and 2-km inner nests to achieve data assimilation

175   over the parent domain. In each of these experiments, the parent domain assimilates the same types

176   of data as are assimilated in the ghost domain 2.

177   Several sets of data assimilation experiments (with and without GMI data) are performed to

178   evaluate the impact of assimilating GMI radiance on hurricane simulations (see the list of

179   experiments in Table 1) using the GSI-based ensemble-3DVAR (GSI hereafter for simplicity) data

180   assimilation system. Each set of experiments consists of a control experiment (CTRL), which

181   assimilates all data (except for the tail Doppler radar data because the data were absent in many

182   cases in this study) that are currently assimilated in operational HWRF, including conventional

183   data, GPS RO data, satellite-derived winds, and satellite radiance observations from both

184   microwave (e.g., AMSU-A, ATMS, MHS, etc) and infrared (e.g., AIRS, IASI, etc.) sensors, and

185   the GMI data assimilation experiment (GMI), which is the same as CTRL but with GMI clear-sky

186   radiance assimilated in the parent domain and ghost domain 2. For all experiments, the HWRF

187   model is spun up by regular 6-hourly analysis-forecast cycles with all the data assimilated into the

188   CTRL experiments (as described above) till 6-h before the data assimilation experiments with GMI.

189   Specifically, for Hurricane Joaquin, the mature phase of its life cycle is emphasized for the

190   experiments in this study. The spin-up period is from 00UTC 29 September 2015 till 00 UTC 1

191   October 2015. Then, the data assimilation experiments are performed in 6-hourly analysis-forecast

192   cycles from 0600 UTC 1 October to 1800 UTC 2 October 2015 with GMI data, with the

193   configurations of CTRL1 and GMI1 in Table 1. For Hurricane Matthew, both the genesis and

194   mature phases are included. For its genesis phase, the spin-up period is from 1200 UTC 26

195   September (when Matthew was still a tropical disturbance) till 1200 UTC 27 September 2016, and

196   the data assimilation experiments (CTRL2 and GMI 2 in Table 1) are performed in 6-hourly

197   analysis-forecast cycles from 1800 UTC 27 September to 0000 UTC 29 September 2016. For its

198   mature phase, the HWRF model is spun up from 1800 UTC 30 September 2016 till 1800 UTC 2

199   October 2016, and the data assimilation experiments (CTRL3 and GMI3 in Table 1) are performed

200   from 0000 UTC 3 October to 1200 UTC 4 October 2016. The 120-h forecasts are performed at

201   each analysis time after the data assimilation.

202   3. GMI data quality control and bias correction

203   *a. Quality control (QC)*

204   The QC for GMI clear-sky radiance in the GSI data assimilation system uses two parameters

205   associated with cloud liquid water (CLW) and cloud ice, and three parameters associated with

206   surface emissivity (following Garrett et al. 2010).

207   First, over the sea surface, a column CLW is computed using measurements from GMI

208   Channels 1 to 7, 12, and 13:

209
$$\text{CLW} = a_{0,\text{clw}} + \sum_{\substack{i=1-7 \\ ,12,13}} c_i \, T_{b,i} + \hat{c}_1 \log(T_{b,3} - T_{b,4}) + \hat{c}_2 \log(T_{b,6} - T_{b,7}) \tag{2}$$

210   where c_i $(i = 1 - 7, 12, 13)$ and $\hat{c}_1 \; and \; \hat{c}_2$ are prescribed regression coefficients, and

211    $T_{b,i}$ $(i = 1 - 7, 12, 13)$ is the GMI brightness temperature at channel i. Another column cloud ice

212   (e.g., graupel water path or GWP) parameter is computed in a similar fashion:

213
$$\text{GWP} = a_{0,\text{gwp}} + \sum_{\substack{i=1-7 \\ ,12,13}} g_i \, T_{b,i} + \hat{g}(300 - \log(T_{b,10})) \tag{3}$$

214   Table 2 summarizes the values of c_i, $\hat{c}_i$, g_i and $\hat{g}$. Constant thresholds of 0.05 are used for both

215   CLW and GWP to toss pixels that are considered to be contaminated by CLW emission and ice

216   scattering.

217   In addition, the GSI surface emissivity QC filters pixels affected by errors in the modeling of

218   surface emissivity using channels that are less susceptible to the emission and absorption of water

219   vapor, e.g., 10.65 Ghz, 18.87 Ghz, and 36.5 Ghz, each of which contributes one emissivity

220   parameter. The emissivity parameters for these channels are calculated from an emissivity

221   regression using all thirteen GMI channel T_b values and the model surface skin temperature. A

222   pixel is considered to be affected by surface emissivity error if any of these three parameters

223   exceeds a corresponding prescribed threshold. Figure 2 shows a sample of the spatial distribution

224   of data from GMI Channel 5 brightness temperatures that pass and fail the QC in the GSI system.

225   *b. Bias Correction (BC)*

226   All data assimilation systems are developed based on the assumption of unbiased Gaussian

227   observational errors. However, for satellite radiance observations, sources of bias can arise from

228 instrument error, such as calibration error and degradation of the instrument over time, systematic

229 modeling error embedded in the radiative transfer model (including the implicit assumptions of

230 the absence of cloud liquid and cloud ice), and variation of the scan angle that causes changes in

231 the field of view at different scan positions. While random error can be handled by the data

232 assimilation system, systematic errors (biases) can ultimately degrade the analysis, as the data

233 assimilation system implicitly assumes an unbiased observational error (Dee 2004; Migliorini

234 2012). Therefore, systematic error has to be removed from the observations before passing them

235 to the data assimilation system.

236   Bias correction for satellite observations consists of two main components: air mass–

237 dependent bias and scan angle–dependent bias. Since GSI Version 3.3, bias correction for these

238 two components has been performed in a single step in the enhanced radiance bias correction

239 framework. Specifically, air mass–dependent bias for each GMI channel j is projected by a

240 weighted linear sum of a static bias term b_j, air mass–dependent predictors $\{p_{i,j}^{(1)}\}$, and scan angle

241 $\{p_{i,j}^{(2)}\}$:

$$b_j = b_{0,j} + \sum_{i=1}^{3} \beta_{i,j}\, p_{i,j}^{(1)}(x) + \sum_{l=1}^{4} \alpha_{l,j}\, \phi^i , \qquad (3)$$

243 where $\beta_{i,j}$ ($i = 1, 2, 3$) and $\alpha_{l,j}$ ($l = 1, ..., 4$) are bias correction coefficients for air mass

244 components and scan angle components, respectively, and ϕ is the field of view number (FOVN).

245 The air mass–dependent predictor $p_{i,j}^{(1)}$ ($i = 1,2,3$) is defined as follows:

$$p_{1,j}^{(1)} = (\cos(\phi))^2 \times \text{CLW} \qquad (4)$$

$$p_{2,j}^{(1)} = \left(\Gamma_j^\tau - \bar{\Gamma}_j^\tau\right)^2 \qquad (5)$$

$$p_{3,j}^{(1)} = \Gamma_j^\tau - \bar{\Gamma}_j^\tau \qquad (6)$$

249 where Γ_j^τ is the lapse rate of transmittance for channel j and varies over pixels, and $\bar{\Gamma}_j^\tau$ is the mean

250　lapse rate of temperature. The Γ_j^τ in (5) and (6) is computed by the following expression:

251
$$\Gamma_j^\tau = -\sum_{k=1}^{K}(\tau_{j,k+1} - \tau_{j,k})(T_{k+1} - T_{k-1}) \,, \qquad (7)$$

252　where $\tau_{j,k}$ is the transmittance from the kth model level to the top of atmosphere for the jth channel

253　and is computed during CRTM integration, while T_k is the temperature at the kth model level.

c. BC coefficients for GMI clear-sky radiances

255　　　　In operational HWRF, bias correction coefficients for each sensor are prescribed in the

256　input GFS files. However, since GMI radiance data had not yet been assimilated in the operational

257　GFS in 2015 and 2016, BC coefficients for GMI radiance observations were not available in these

258　input data. Therefore, in this study, the BC coefficients for GMI radiances are derived

259　independently using a combination of a static BC method and the adaptive BC capability within

260　GSI. Specifically, a rough estimation of the BC coefficients is computed using a linear regression

261　on a representative set of observations minus forecasts (O-F) derived from 14 days of GMI

262　overpasses in the region of interest. This rough estimation of coefficients is then treated as an

263　initial guess for a variational BC inside of GSI through an iteration process over a short period of

264　data assimilation cycles (e.g., following Zhu et al. 2014) to obtain the temporal variation of the

265　coefficients.

266　　　　First, for each hurricane case, a set of 14-day overpass GMI data over the corresponding

267　basin (North Atlantic Ocean for hurricanes Joaquin and Matthew) is collected, which spans from

268　the genesis phase to the decay phase of the hurricane. Meanwhile, for each GMI overpass, the

269　departure between the simulated and observed T_b (e.g., observed – first guess, or O-F) and the

270　predictors (e.g., CLW, temperature lapse rate [T_{lap}] and its square, four orders of scan angles, mean

271　bias or constant offsets) for each pixel are calculated. A multilinear regression is then used to

272　estimate the dependence of O-F values on a set of predictors and the BC coefficients are computed.

11

273   Figure 3 shows sample results of the dependence of O-F on predictors based on statistics during

274   the life of Hurricane Joaquin (between 26 September and 9 October 2015) for Channels 3, 5, 6, 8,

275   and 10. There is apparent dependence between O-F and the CLW and temperature lapse rate (Tlap),

276   respectively, with biases present, but there is no dependence between O-F and the scan angles.

277   As mentioned, the current version of GSI uses variational bias correction to adaptively

278   update the BC coefficients by including the coefficients as analysis variables in the data

279   assimilation step. This advancement allows the data assimilation system to adjust the BC

280   coefficients automatically at each analysis step and capture the temporal evolution of the

281   coefficients effectively (Zhu et al. 2014). Using this capability of the GSI system, a GSI iteration

282   experiment is performed to fine-tune the BC coefficients for different phases of the hurricane case

283   studies. Details of the iteration procedure are as follows: First, for a given hurricane (e.g., Joaquin),

284   at least 4 6-hourly data assimilation analysis-forecast cycles (each of which has at least one GMI

285   overpass near the hurricane region) are performed. Then, using the BC coefficients obtained from

286   linear regression as an initial guess, GSI analysis is performed sequentially at each of these 6-

287   hourly analysis-forecast cycles. At each GSI analysis, the BC coefficients are adjusted accordingly

288   and then passed to the next analysis-forecast cycle. After the coefficients go through all data

289   assimilation within the analysis window, one iteration is completed and the whole process is

290   repeated again for the next iteration until the coefficients stabilize. Figure 4 shows the variation of

291   various predictors during the iteration procedure. It shows that the BC coefficients are stable after

292   only several iterations for most variables. In fact, if the linear regression step is eliminated and

293   the variational bias correction alone is used, the bias coefficients will converge (or become stable)

294   slowly and can take more than 50 iterations to reach similar results. Zhu et al (2014) have noted

295   that poor initial guesses of BC coefficients may lead the QC to reject/accept data of good/poor

296 quality.

297   Figure 5 summarizes the O-F statistics before and after bias correction. The data sample

298 consists of assimilated GMI observations from the first 4 analysis-forecast cycles in the GMI data

299 assimilation experiment during the mature phase of Joaquin in HWRF d01. The comparison shows

300 that before BC, O-F dependence on CLW follows the same trend shown in the left column of

301 Figure 3. After BC, O-F values are distributed almost uniformly over the entire range of CLW

302 values. This indicates that the BC coefficients obtained from the two-step bias correction approach

303 are able to remove bias arising from CLW emission. In addition, the right column of Figure 5

304 shows a histogram of the first-guess departure before and after BC, revealing that after BC, O-F

305 distribution become less biased with a normal distribution around zero.

306 # 4. Impact of GMI radiance data on numerical simulations of hurricanes

307 *a. Track and intensity*

308 1) HURRICANE JOAQUIN

309   The track forecast of Hurricane Joaquin in 2015 was challenging for the forecast community.

310 As Joaquin reached category 3 strength and became a major hurricane on 1 October 2015, it made

311 a hairpin turn and moved northeast under the influence of a deepening mid- to upper-level trough

312 near the southeastern United States. As mentioned in the Section 2c, the data assimilation

313 experiments are performed from 0600 UTC 1 October to 1800 UTC 2 October (see Table 1) in 6-

314 hourly analysis-forecast cycles. A 120-h forecast is made at each analysis time of these 6-h

315 analysis-forecast cycles after the data assimilation.

316   Figure 6 illustrates a comparison of the aggregated track forecasts between CTRL1 (without

317 assimilation of GMI data) and GMI1 (with assimilation of GMI data) during the cycling periods

318 from 0600 UTC 1 October to 1800 UTC 2 October 2015. From Figure 6a, it is clear that the CTRL1

319 experiment shows systematic biases of forecast tracks toward the northwest side of the best track

320 during the hairpin turn of Joaquin. These track errors are greatly reduced for experiments initiated

321 after 0600 UTC 2 October, as the hairpin turn is close to completion. In contrast, GMI1 (Figure

322 6b) also shows a great reduction in the magnitude of the track biases, owing to the assimilation of

323 the GMI data. The largest difference in track forecasts between CTRL1 and GMI1 is found for the

324 forecasts initiated at 0000 UTC 2 October. During the first 12-hour forecasts, tracks from both the

325 CTRL1 and GMI1 experiments show good agreement with the best track. However, the tracks in

326 CTRL1 show a more northward trend soon after, while those in GMI1 attain a more realistic

327 eastward propagation. Track errors of CTRL1 exceed 200 km after 30 hours of forecast, while

328 GMI1 retains a track error of less than 140 km throughout the 72-h forecast period.

329   The 120-hour mean track error for CTRL1 and GMI1 (as shown in Figures 6a and b), averaged

330 over the forecasts started from each analysis of all 7 analysis-forecast cycles against the NHC best-

331 track data, is shown in Figure 6c. A consistent improvement in the track forecast is seen after the

332 assimilation of GMI data, with roughly 20% and more than 12% reductions in track error during

333 the first 72-h and over the entire 120-h forecasts, respectively.

334   Figure 7 shows a comparison of the minimum SLP and maximum surface wind forecasts

335 between CTRL1 and GMI1 from all 7 different forecast lead times. The figure indicated an overall

336 positive or neutral impact of GMI data assimilation on the intensity forecast for Hurricane Joaquin

337 over 120 h forecasts, while positive impacts on the intensity forecasts at first 60-h are evident.

338   Figures 8a and b show the spatial distribution of assimilated brightness temperature from all

339 microwave sensors (GMI data are highlighted in purple) over HWRF d01 at two different analysis

340 times in GMI1. Except for GMI data, a set of microwave sounders, including the Advanced

341 Microwave Sounding Unit-A (AMSU-A) onboard NOAA-15, NOAA-19, and METOP-A

342   satellites, the Microwave Humidity Sensor (MHS) onboard NOAA-18, NOAA-19, and METOP-

343   A satellites, and the Advanced Technology Microwave Sounder (ATMS) is assimilated. In each

344   of the times shown in Figures 8a and b, GMI contains an overpass in the near-hurricane

345   environment, where overpasses of other similar sensors are not present. This shows that the

346   addition of GMI data to the entire pool of microwave sensors can provide more complete coverage

347   of microwave satellite observations in the near-hurricane environment.

348   A comparison of GMI1 with CTRL1 shows that the impacts of assimilating GMI clear-sky

349   radiance on the intensity forecast of Joaquin are less significant. The 60-hour mean error in the

350   maximum wind and minimum central sea level pressure (SLP) forecasts shows either neutral or

351   marginal impacts (with less than 5% error reduction) from the assimilation of GMI data for most

352   of the forecast time (Figure not shown).

353   2) HURRICANE MATTHEW

354   Compared to Joaquin, Hurricane Matthew exhibited *less* uncertainty in its track throughout its

355   life cycle. Both the genesis and mature phases of Matthew are used to further examine the impact

356   of assimilating GMI data on track and intensity forecasts (see experimental design in Table 1).

357   Figure 9 and 10 show comparisons of the track, minimum SLP, maximum wind forecasts between

358   CTRL2 and GMI2 from different forecast lead times at the genesis, rapid intensification, and part

359   of intensity change phases of Matthew from 1800 UTC 27 Sep to 0500 UTC Oct 2016. Figure 9

360   indicated a small, neutral impact of assimilation of GMI data on the track forecast of Hurricane

361   Matthew. However, Figure 10 reveals an obvious positive impact of GMI data assimilation on the

362   intensity forecast with improvements in the first 60-h forecasts (up to 0000 UTC 1 Oct 2016).

363   Specifically, it is apparent that CTRL2 (without GMI data assimilation) consistently undergoes

364   rapid intensification too early, generally about 12 to 18 hours ahead of the best-track data (Figure

365   10a). In contrast, GMI2 shows a correction in the forecast of minimum SLP (Figure 10b) during

366   the rapid intensification period. However, after 0000 UTC 1 Oct 2016, the end of Matthew's rapid

367   intensification, the GMI data assimilation results in mixed forecast impacts with slightly degraded

368   intensity forecast in some cases, reflecting the complicated dynamic and physical processes

369   involved in the intensity changes. Nevertheless, the influences of the initial conditions on forecasts

370   should not be as significant as the physical processes after 60 hours forecasts. Figure 10c displays

371   the mean 120-h minimum SLP and maximum wind forecast errors. Overall, the assimilation of

372   GMI data results in consistent positive impacts on both minimum SLP and maximum surface

373   wind (MSW) for the first 60-h forecast while some mixed impacts afterward, although the overall

374   averaged impacts during the 120-h forecast period are positive.

375   The mature phase of Matthew exhibits small uncertainty in both track and intensity forecasts.

376   Figure 11 shows the 60-h mean track and intensity forecast, which covers the mature phase of

377   Matthew but not the intensity change period afterward for experiments CTRL3 and GMI3. Overall,

378   the assimilation of GMI clear-sky radiance has a neutral impact for the mature phase of Matthew.

379   *b. Impacts on hurricane large-scale environmental conditions*

380   Further diagnoses are conducted to demonstrate the impact of GMI data assimilation on

381   the hurricane environment. Figure 12 shows geopotential height and streamline fields at 550 hPa

382   and 750 hPa at the 42-h forecasts for Joaquin from the CTRL1 and GMI1 experiments (valid at

383   1800 UTC 3 October 2015), respectively, compared with the corresponding ECMWF-interim

384   reanalysis at the valid time. While the overall environmental features are similar between the

385   CTRL1 and GMI1 experiments, noticeable differences are seen on the northwest side of the

386   simulated vortices. Specifically, throughout the layer from 500 to 800 mb, the flow around the

387   vortex in GMI1 is more isolated from the deepening mid- to upper-level trough (on the northwest

388   side of the hurricane) than that of CTRL, similar to a separation seen in the ECMWF reanalysis

389   field.

390   *c. Impacts on forecasts of hurricane structure: against dropsonde sounding during TCI*

391   To further verify the impact of GMI data assimilation on hurricane forecasts, independent

392   observations—namely, soundings obtained from a recent field program, the Tropical Cyclone

393   Intensity (TCI) Experiment—are used. TCI is a collaborative field experiment sponsored by the

394   Office of Naval Research (ONR), with the objective of improving forecasts of tropical cyclone

395   intensity and structure changes (Doyle et al. 2017). During TCI, the NASA WB-57, which carries

396   the High Definition Sounding System (HDSS) Dropsondes, is employed to sample the hurricane

397   inner-core structure and its surrounding environment. The following verification utilizes

398   dropsonde data collected during the mature phase of Joaquin from the HDSS.

399   Because many TCI soundings are taken close to the hurricane center (within 50 km of the

400   center), choosing model profiles that have the same geophysical location as the sounding could

401   result in significant overestimation of errors due to errors in the track forecast in each experiment.

402   To account for this effect, model profiles in each experiment are selected such that their positions

403   relative to the center of the simulated vortices are the same as the position of the soundings relative

404   to the best-track hurricane center. This guarantees that the focus of comparison is on the overall

405   inner-core structure. Figure 13 shows the distribution of TCI soundings around 1800 UTC 2

406   October 2015 and the corresponding model verification grids (from 12-hour forecasts initiated at

407   0600 UTC 2 October 2015). While the vortex center in GMI1 has a geophysical location similar

408   to that of the best-track data, CTRL1 has a track error of roughly 40 km. Apparently, comparing

409   soundings with model profiles at the same geophysical locations (indicated by black circles) is

410   relatively unfair to CTRL1. Instead, model profiles that have the same relative positions with

411 respect to the simulated vortices are more reasonable.

412   Figure 14 reveals the results of comparing the vertical profiles of root mean square error

413 (RMSE) and bias in temperature and specific humidity against TCI dropsonde soundings. In the

414 comparison, only soundings that are within 150 km of the hurricane center are included. The

415 sample contains forecasts initiated at 0600 UTC 2 October and 1200 UTC 2 October 2015, verified

416 against TCI soundings launched around 1800 UTC 2 October and 1800 UTC 3 October, giving a

417 total sample size of 156. From the RMSE in Figures 14a and b, the assimilation of GMI clear-sky

418 radiance reduces error in temperature throughout the entire troposphere, while its impact on

419 specific humidity lies mostly in the mid-troposphere (400 to 700 mb, Figure 14b). Figures 14c and

420 d show the mean bias and the standard deviation of temperature and specific humidity at different

421 pressure levels. For temperature, both experiments (CTRL1 and GMI1) produce warm biases in

422 the lower troposphere (below 500 hPa) and cold bias in the upper troposphere (Figure 14c).

423 However, these biases in GMI1 are noticeably smaller than that in CTRL1. For specific humidity,

424 GMI data also result in reduction of the biases.

425   The impact of GMI on the wind field is also examined. Figures 14e-h show the comparison of

426 RMSE for radial wind and tangential wind between CTRL1 and GMI1 verified against TCI

427 soundings, respectively. Within a 150-km radius of the hurricane center, the wind magnitudes from

428 both CTRL1 and GMI1 are greater than the dropsonde data at the lower levels (below 700 hPa

429 pressure levels), while GMI data assimilation improves the radial wind fields and results in a

430 neutral impact on tangential winds in middle and upper levels (Figure 14 e-f). The comparison is

431 also revealed on the near-hurricane environment within a radius of between 150 and 600 km from

432 the center, giving a sample size of 114. From Figures 14 g and h, it is found that assimilation of

433 the GMI data results in noticeable improvements in the radial wind fields in both the lower

434   troposphere (between 600 and 800 mb) and upper troposphere (about 300 mb), as shown in Figure

435   14g. In terms of tangential velocity (Figure 14h), the impact of GMI is rather neutral, with some

436   positive impact on the mid-level troposphere (between 350 and 450 mb).

437   *d. Impact on temperature and moisture fields during the genesis of Matthew*

438   Assimilation of GMI clear-sky radiance is found to provide noticeable improvements in

439   the intensity forecast of the genesis phase of Matthew. During this phase, it is found that

440   widespread cold air dominates the middle to lower troposphere in the east sector of the storm, as

441   shown by the GFS analysis between 650 mb and 850 mb. Figure 15 compares HWRF 30-h

442   forecasts valid at 0800 UTC 29 September 2016 against the corresponding GFS analysis. It shows

443   that both CTRL2 and GMI2 have a similar east-west temperature gradient across the storm in the

444   mid-troposphere. However, in CTRL2 the cold temperature on the east side of the storm is

445   noticeably weaker compared to the GFS analysis. In contrast, GMI2 has more dominant cold air

446   accumulated in the east sector of the storm, resembling the cold air configuration seen in the GFS

447   analysis, even though the magnitude and spread are still underestimated.

448   Figure 16 shows the vertical profiles of RMSE for temperature and specific humidity

449   within a 600-km radius of the observed storm center, averaged over 30-h forecasts from each

450   analysis of all analysis-forecast cycles of the genesis of Matthew (CTRL2 and GMI2). For the

451   errors in the temperature field, assimilation of GMI data has a positive impact throughout almost

452   the entire troposphere, especially below the 600 hPa pressure level. For specific humidity, obvious

453   error reduction can be seen around the 500 hPa pressure level.

454   In fact, during the genesis phase of Matthew, GMI overpasses are overlapped with other

455   microwave sensors that have similar humidity profiling channels, including AMSU-A, MHS, and

456   ATMS, as shown in Figures 8c and d. These sensors have humidity sensor channels similar to

19

457   those of GMI near 23.8 GHz and 183 GHz. To further investigate the impact of GMI on HWRF

458   forecasts in this type of case, another set of experiments is conducted, called Base and Base+GMI

459   in Table 1. The Base is similar to CTRL2, expect no satellite observations are assimilated. GMI

460   clear-sky radiance is assimilated in Base+GMI, along with other data are assimilated into the Base,

461   including conventional observations, GPS-RO data, and satellite-retrieved wind. In addition,

462   considering the early results of CTRL2 and GMI2 (Figure 10), the evaluation of forecast impacts

463   is conducted for the first 60 h forecasts to emphasize Matthew's genesis and rapid intensification

464   phases only, and also to obtain the clear influences of data assimilation (e.g., initial conditions)

465   that are commonly best shown in the short-range forecasts.

466   Figure 17 shows a comparison of 500- to 850-mb averaged RMSE of specific humidity

467   forecasts between CTRL2, GMI2, Base, and Base+GMI. Figures 17 a and b show that CTRL2 and

468   GMI2 have a rather similar spatial distribution of specific humidity RMSE. Clearly, assimilating

469   GMI clear-sky radiance provides only a small improvement in the moisture field, which is

470   consistent with the result shown in Figure 17b. In Figure 17c, when no radiance observation is

471   assimilated, the Base experiment shows the largest error in the moisture field among all 4

472   experiments, especially on both the northeast and northwest sides of the storm. When GMI data

473   are added, Base+GMI shows a noticeable reduction in RMSE in specific humidity compared to

474   the Base experiment, as shown in Figure 17d, which reveals the sole impact of GMI data

475   assimilation on the specific humidity when other similar satellite sensors are not present. In

476   addition, a comparison of Figure 17d with Figures 17a and b shows that the overall spatial

477   distribution of RMSE in Base+GMI is similar to that in CTRL2 and GMI2, indicating that the

478   constraints imposed by GMI data assimilation on specific humidity are consistent with other

479   sensors, hence resulting in a similar improvement.

480   Figure 18 shows the mean errors for minimum SLP, MSW, and track forecasts in Base and

481   Base+GMI, averaged over the forecasts from the analyses of all the analysis-forecast cycles. It is

482   found that without the presence of other sensors, the assimilation of GMI clear-sky radiance alone

483   is also able to provide similar positive impacts on HWRF forecasts during Matthew's genesis

484   phase.

5. Summary and concluding remarks

486   This study examines the impact of assimilating GMI clear-sky radiance on HWRF hurricane

487   forecasts using the GSI-based hybrid ensemble-3DVar data assimilation system. Prior to

488   assimilating the radiance, bias corrections are conducted using a two-step approach. First, a static

489   bias correction is used to derive a rough estimate of the bias correction coefficient using regression

490   on a representative sample of radiance departure. The estimated bias correction coefficients are

491   then treated as a first guess to go through a series of iterative procedures using the variational bias

492   correction capability in GSI to capture the small-time variation of the coefficients.

493   Hurricane Joaquin in 2015 and Matthew in 2016 are used as case studies to evaluate the

494   impact of assimilating GPM-GMI clear-sky radiance on hurricane analysis and forecasts. For the

495   mature phase of Joaquin, assimilating GMI radiance results in significant improvement in the track

496   forecast, especially during its hairpin turn. Comparing against ECMWF-interim data, we found a

497   significant improvement in the forecast of the geopotential height field in the near-hurricane

498   environment, leading to a more realistic interaction between the simulated hurricane vortex and

499   the nearby mid- to upper-level trough. The overall impact on the intensity forecast of the mature

500   phase of Joaquin is significant in short-range (60-h) but relatively modest over 120-h forecasts.

501   This is mostly due to the fact that clear-sky radiance observations occur away from the inner-core

502   region of the hurricane.

503   For the genesis phase of Matthew, forecast results show that assimilating GMI radiance

504   improves the intensity forecast, especially during the first 48- to 60-hour forecast. Close

505   examination of the forecast result using GFS analysis shows that assimilating GMI clear-sky

506   radiance improves the forecast of mid- to lower-level cold air aggregated on the northeast side of

507   the storm, which causes Matthew's intensification to slow down. Using GFS analysis as reference,

508   the overall RMSE statistics show a clear improvement in temperature throughout the entire

509   troposphere and in low- to mid-level specific humidity in the near-hurricane environment (radius

510   less than 500 km), even when other microwave sounders are present (e.g., AMSU-A, ATMS, MHS,

511   etc.).

512   An additional experiment is performed for the mature phases of Matthew, during which

513   Matthew exhibits relatively small uncertainty in both track and intensity. The overall result of this

514   phase shows that while the impact of GMI on both track and intensity is rather small, no negative

515   impact is seen.

516   The experiments performed in this study indicate that there is a great potential to assimilate

517   GMI satellite radiances into the regional hurricane prediction models (e.g., HWRF) to improve the

518   operational hurricane prediction. However, numerical experiments from this paper did not fully

519   follow the operational HWRF analysis and forecast procedures (e.g., no tail Doppler radar data

520   assimilation; no vortex intensity correction; with the emphasis on short-range forecasts only, etc.).

521   Meanwhile, the operational HWRF model has been updated at the time when this paper was written.

522   Therefore, future work will further examine the impacts of GMI data assimilation on operational

523   HWRF hurricane analyses and forecasts and achieve the statistical significance. The investigation

524   will also extend to assimilating GMI all-sky radiance, especially in the hurricane inner-core

525   regions. Moreover, although the two-step bias correction methods in this study shed light on bias

22

526   correction in the regional model, additional efforts still required to address the issue adequately in

527   the hurricane environment.

528   ***Acknowledgments:***

536

References

538 Aravéquia, J. A., I. Szunyogh, E. J. Fertig, E. Kalnay, D. Kuhl, and E. J. Kostelich, 2011:

539   Evaluation of a strategy for the assimilation of satellite radiance observations with the

540   local ensemble transform Kalman filter. *Mon. Wea. Rev.*, **139**, 1932–1951,

541   doi:10.1175/2010MWR3515.1.

542 Bauer, P., P. Lopez, A. Benedetti, D. Salmond, and E. Moreau, 2006: Implementation of 1D4D

543   -Var assimilation of precipitation affected microwave radiances at ECMWF. I: 1D-Var.

544   *Quart. J. Roy. Meteor. Soc.*, **132**, 2277–2306.

545 Berg, R., 2016: Tropical Cyclone Report Hurricane Joaquin (AL112015) 28 September–7

546   October 2015, *National Oceanic and Atmospheric Administration – National Hurricane*

547   *Center*. [available on web link http://www.nhc.noaa.gov]

548 Biswas, M. K., L. Carson, C. Holt, and L. Bernardet, 2015: Community HWRF Users' Guide

549   V3.7a,152pp. [available online at

550   http://www.dtcenter.org/HurrWRF/users/docs/users_guide/HWRF_v3.7a_UG.pdf]

551 Dee, D. P., 2004: Variational bias correction of radiance data in the ECMWF system. Proc.

552   *ECMWF Workshop on Assimilation of High Spectral Resolution Sounders in NWP*,

553   Reading, United Kingdom, ECMWF, 97–112.

554 Derber, J. C., and W.-S. Wu, 1998: The use of TOVS cloud-cleared radiances in the NCEP SSI

555   analysis system. Mon. Wea. Rev.,126, 2287–2299.

556 Doyle, J., J. Moskaitis, J. Feldmeier, R. Ferek, M. Beaubien, M. Bell, D. Cecil, R. Creasey,

557   P. Duran, R. Elsberry, W. Komaromi, J. Molinari, D. Ryglicki, D. Stern, C. Velden, X.

558   Wang, T. Allen, B. Barrett, P. Black, J. Dunion, K. Emanuel, P. Harr, L. Harrison, E.

559   Hendricks, D. Herndon, W. Jeffries, S. Majumdar, J. Moore, Z. Pu, R. Rogers, E.

560   Sanabia, G. Tripoli, and D. Zhang, 2017: A view of tropical cyclones from above: The

561   Tropical Cyclone Intensity (TCI) experiment. *Bull. Amer. Meteor. Soc.*,

562   doi:10.1175/BAMS-D-16-0055.1, in press.

563   Garrett, K., L. Moy, F. Iturbide-Sanchez, S.-A. Boukabara, 2010: A physically-based rainfall rate

564   algorithm for the Global Precipitation Mission. 5th IPWG Workshop, Hamburg,

565   Germany, October 11-15, 2010.

566   Goerss, J., 2009: Impact of satellite observations on the tropical cyclone track forecasts of the

567   NOGAPS. *Mon. Wea. Rev.*, **137**, 41–50.

568   Gopalakrishnan, S. G., F. Marks, X. Zhang, J.-W. Bao, K.-S. Yeh, and R. Atlas, 2011: The

569   Experimental HWRF System: A study on the influence of horizontal resolution on the

570   structure and intensity changes in tropical cyclones using an idealized framework. *Mon.*

571   *Wea. Rev.*, **139**, 1762–1784, doi:10.1175/2010MWR3535.1.

572   Han, Y., P. van Delst, Q. Liu, F. Weng, B. Yan, R. Treadon, and J. Derber, 2006: *JCSDA*

573   *Community   Radiative Transfer Model (CRTM)—version 1.* NOAA Tech. Rep., NESDIS

574   122, 40 pp.

575   Hoppel, K. W., S. D. Eckermann, L. Coy, G. E. Nedoluha, D. R. Allen, S. D. Swadley, and N. L.

576   Baker, 2013: Evaluation of SSMIS upper atmosphere sounding channels for high altitude

577   data assimilation. *Mon. Wea. Rev.,* **141**, 3314–3330, doi:10.1175/MWR-D-13-00003.1.

578   Hou, A. Y., and Coauthors, 2014: The Global Precipitation Measurement mission. *Bull. Amer.*

579   *Meteor. Soc.*, **95**, 701–722, doi:10.1175/BAMS-D-13-00164.1

580   Kazumori, M., 2014: Satellite radiance assimilation in the JMA operational mesoscale 4DVAR

581   system. *Mon. Wea. Rev.*, **142**, 1361–1381.

582   Lin, H., S. S. Weygandt, S. G. Benjamin, and M. Hu, 2017: Satellite radiance data assimilation

583   within the hourly updated rapid refresh. *Wea. Forecasting*, 1273-1287.

584   Liu, Q., N. Surgi, S. Lord, W.-S. Wu, S. Parrish, S. Gopalakrishnan, J. Waldrop,

585   and J. Gamache, 2006: Hurricane initialization in HWRF model. *27th Conf. on*

586   *Hurricanes and Tropical Meteorology*, Monterey, CA, Amer. Meteor. Soc., 8A.2.

587   [Available online

588   at https://ams.confex.com/ams/27Hurricanes/techprogram/paper_108496.htm.]

589   Liu, Z., C. S. Schwartz, C. Snyder, and S.-Y. Ha, 2012: Impact of assimilating AMSU-A radiances

590   on forecasts of 2008 Atlantic tropical cyclones initialized with a limited-area ensemble

591   Kalman filter. *Mon. Wea. Rev.*, **140**, 4017–4034.

592   McNally, P., J. C. Derber, W. Wu, and B. B. Katz, 2000: The use of TOVS level-1b radiances in

593   the NCEP SSI analysis system. *Quart. J. Roy. Meteor. Soc.*, **126**, 689–724.

594   Migliorini, S., 2012: On the equivalence between radiance and retrieval assimilation. *Mon. Wea.*

595   *Rev.*, **140**, 258–265.

596   Miyoshi, T., and Y. Sato, 2007: Assimilating satellite radiances with a local ensemble transform

597   Kalman filter (LETKF) applied to the JMA global model (GSM). *SOLA*, **3**, 37–40.

598   Okamoto, K., and J. C. Derber, 2006: Assimilation of SSM/I radiances in the NCEP global data

599   assimilation system. *Mon. Wea. Rev.*, 134, 2612–2631.

600   Pu, Z., W.-K. Tao, S. Braun, J. Simpson, Y. Jia, J. Halverson, A. Hou, and W. Olson, 2002: The

601   impact of TRMM data on mesoscale numerical simulation of Supertyphoon Paka. *Mon.*

602   *Wea. Rev.* 130, 2248-2258

603   Pu, Z., X. Li, C. Velden,S. Aberson, W. T. Liu, 2008: Impact of aircraft dropsonde and satellite

604   wind data on the numerical simulation of two landfalling tropical storms during

605   TCSP . *Wea. Forecasting* 23, 62-79.

606   Pu, Z., and L. Zhang, 2010: Validation of AIRS temperature and moisture profiles over tropical

607   oceans and their impact on numerical simulations of tropical cyclones, *J. Geophys.*

608   *Res.*, 115 , D24114, doi:10.1029/2010JD014258

609   Pu, Z., S. Zhang, M. Tong and V. Tallapragada. 2016: Influence of the self-consistent regional

610   ensemble background error covariance on hurricane inner-core data assimilation with the

611   GSI-based hybrid system for HWRF, *J. Atmos. Sci.*, 73, 4911-4925.

612   http://dx.doi.org/10.1175/JAS-D-16-0017.1

613   Qin, Z., X. Zou, and F. Weng, 2013: Evaluating added benefits of assimilating GOES imager

614   radiance data in GSI for coastal QPFs. *Mon. Wea. Rev.*, **141**, 75–92, doi:10.1175/ MWR

615   -D-12-00079.1.

616   Sakamoto, M., and J. R. Christy, 2009: The influences of TOVS radiance assimilation on

617   temperature and moisture tendencies in JRA-25 and ERA-40. *J. Atmos. Oceanic Technol.*,

618   **26**, 1435–1455.

619   Tallapragada, V., and Coauthors, 2015: Hurricane Weather Research and Forecasting (HWRF)

620   Model: 2015 scientific documentation. NCAR Development Testbed Center Rep., 119

621   pp. [Available online at http://nldr.library.ucar.edu/collections/technotes/TECH-NOTE-

622   000-000-000-893.pdf .]

623   Wang,P., J. Li, M. D. Goldberg, T. J. Schmit, A. H. N. Lim, Z. Li, H. Han, J., S. A. Ackerman,

624   2015: Assimilation of thermodynamic information from advanced infrared sounders

625   under partially cloudy skies for regional NWP, *J. Geophy. Res.: Atmospheres*, **120**, 11,

626   5469

627   Weng, F., 2007: Advances in radiative transfer modeling in support of satellite data assimilation.

628   *J. Atmos. Sci.*, **64**, 3799–3807.

629   Wu, T.-C., M. Zupanski, L. D. Grasso, P. J. Brown, C. D. Kummerow, and J. A. Kna , 2016: The GSI

630   capability to assimilate TRMM and GPM hydrometeor retrievals in HWRF. *Q. J. Roy. Meteor.*

631   *Soc.*, **142**, 2768-2787

632 Xu, D., Z. Liu, X.-Y. Huang, J. Min, and H. Wang, 2013: Impact of assimilating IASI radiance

633   observations on forecasts of two tropical cyclones. *Meteor. Atmos. Phys.*, **122**, 1–18,

634   doi:10.1007/s00703-013-0276-2.

635 Xu, D., J. Min, F. Shen, J. Ban, and P. Chen, 2016: Assimilation of MWHS radiance data from

636   the FY-3B satellite with the WRF Hybrid-3DVAR system for the forecasting of binary

637   typhoons. *J. Adv. Model. Earth Syst.*, **8**, 1014–1028, doi:10.1002/2016MS000674.

638 Yang, C., Z. Liu, J. Bresch, S. R. H. Rizvi, X.-yu Huang, and J. Min, 2016: AMSR2 all-sky

639   radiance assimilation and its impact on the analysis and forecast of Hurricane Sandy with

640   a limited-area data assimilation system. *Tellus A*, **68**, 30917, doi:10.3402/tellusa.v68.30917.

641 Zhang, H. and Z. Pu, 2014: Influence of assimilating surface observations on the prediction of

642   landfalls of Hurricane Katrina (2005) with ensemble Kalman filter. *Mon. Wea.*

643   *Rev.*, **142** , 2915-2934. doi: http://dx.doi.org/10.1175/MWR-D-14-00014.1

644 Zhang, M., M. Zupanski, M.-J. Kim, and J. A. Knaff, 2013: Assimilating AMSU-A radiances in

645   the TC core area with NOAA operational HWRF (2011) and a hybrid data assimilation

646   system: Danielle (2010). *Mon. Wea. Rev.*, **141**, 3889–3907. doi:10.1175/MWR-D-12-

647   00340.1

648 Zhang, S. Q., M. Zupanski, A. Y. Hou, X. Lin, and S. H. Cheung, 2013: Assimilation of

649   precipitation-affected radiances in a cloud-resolving WRF ensemble data assimilation

650   system. *Mon. Wea. Rev.*, **141**, 754–772, doi:10.1175/MWR-D-12-00055.1.

651 Zhu, Y., J. Derber, A. Collard, D. Dee, R. Treadon, G. Gayno, and J. A. Jung, 2014:

652   Enhanced radiance bias correction in the National Centers for Environmental

653   Prediction's Gridpoint Statistical Interpolation data assimilation system. *Q.J.R. Meteorol.*

654   *Soc.*, **140**, 1479–1492.

655 Zou, X., Z. Qin, and F. Weng, 2011: Improved coastal precipitation forecasts with direct

656   assimilation of GOES 11/12 imager radiances. *Mon. Wea. Rev.*, **139**, 3711–3729,

657   doi:10.1175/ MWR-D-10-05040.1.

658 Zou, X., F. Weng, B. Zhang, L. Lin, Z. Qin, and V. Tallapragada, 2013: Impacts of assimilation

659   of ATMS data in HWRF on track and intensity forecasts of 2012 four landfall hurricanes.

660   *J. Geophys. Res. Atmos.*, **118**, 11 558–11 576, doi:10.1002/2013JD020405.

661

662

Figure Captions

664 **Figure 1.** GFS analysis of sea level pressure (color contours, units hPa) and storm center from

665 NHC best track (black storm sign) at 0000 UTC 2 October 2015 for Hurricane Joaquin. HWRF

666 model forecast domains, as indicated by d01, d02, and d03, and HWRF data assimilation domains,

667 as indicated by ghost d02 (black shaded area) and ghost d03 (pink shaded area), are also indicated.

668 **Figure 2**: Spatial distribution of (a) GMI overpass over ghost d02 at 0000 UTC 2 October 2015,

669 with data that passed QC (colored with O-F values) and failed QC (gray), and (b) GMI

670 observations that failed QC shaded with different colors to denote the type of failure (blue: CLW

671 QC; green: GWP QC; red: emissivity QC). Ghost d02 is shown as an inner domain inside a

672 longitude-latitude box. The hurricane center is indicated by the black cross at the domain center.

673 **Figure 3**: Two-dimensional histogram showing the dependence of the O-F sample (collected from

674 26 September 2015 to 9 October 2015) on CLW (left column, (kg/m^2)), Tlap (middle column, (K)),

675 and the field of view number (FOVN, right column, (rad)) for Channels 3, 5, 6, 8, and 10. The y-

676 axis denotes the O-F value, and the x-axis represents the predictor. The flat distribution around 0

677 is unbiased.

678 **Figure 4**: Variation of BC coefficients with the iteration number obtained from experiment GMI1

679 for (a) constant offset, (b) CLW predictor (CLW), (c) transmittance lapse rate (Tlap), and (d) scan

680 angle.

681 **Figure 5**: O-F statistics against CLW predictor before (left) and after BC (middle). Histogram of

682 O-F values is shown in the right column. Data sample consists of assimilated GMI observations

683 from 4 analysis-forecast cycles of the mature phase of Joaquin that have major GMI overpasses in

684 the parent domain (0600 UTC 1 October, 1800 UTC 1 October, 0200 UTC 2 October, and 0600

685 UTC 2 October 2015).

686 **Figure 6**: Comparison of tracks between NHC best track (black curve) with 120-h HWRF

687 forecasts (colored lines) initialed by each of the analyses generated in the 7 analysis-forecast cycles

688 (as listed in the legend) for experiments without and with GMI data assimilation for (a) CTRL1

689 and (b) GMI1. (c) is the 120-h mean track error averaged over the all 7 forecasts in (a) and (b), for

690 CTRL1 (red) and GMI1 (blue).

691 **Figure 7**: Aggregated minimum SLP and maximum surface wind forecasts of (a and c) CTRL1

692 and (b and d) GMI1 (colored curves) compared with NHC best-track data (black curve; 06 UTC

693 UTC 01 Oct to 1800 UTC 07 Oct 2015) for the 120-h forecast started at the analysis time in all 7

694 analysis-forecast cycles (as listed in the legend). (e) and (f) show mean forecast errors of minimum

695 sea level pressure and maximum surface wind averaged over the forecasts started at the analysis

696 time in all 6 analysis-forecast cycles (6-hourly from 06 UTC 01 Oct to 18 UTC 02 Oct 2015) for

697 CTRL1 (red) and GMI1 (blue). In (e) and (f), the colored numbers on the left and right show the

698 averaged errors over all 7 forecasts in first 60h and 120h HWRF integration, respectively.

699 **Figure 8**: Assimilated brightness temperature observations of all microwave sensors during the

700 mature phase of Joaquin at (a) 0600 UTC 1 October and (b) 0600 UTC 2 October 2015, and during

701 the mature phase of Matthew at (c) 1800 UTC 27 September and (d) 1200 UTC 28 September

702 2016. GMI overpasses are highlighted in purple.

703 **Figure 9**: Comparison of tracks between NHC best track (black curve) with 120-h HWRF

704 forecasts (colored lines) initialed by each of the analyses generated in the 6 analysis-forecast cycles

705 (as listed in the legend) for experiments without and with GM2 data assimilation for (a) CTRL2

706 and (b) GMI2. (c) is the 120-h mean track error averaged over the all 6 forecasts in (a) and (b), for

707 CTRL2 (red) and GMI2 (blue).

708 **Figure 10**: Aggregated minimum SLP and maximum surface wind forecasts of (a and c) CTRL2

31

709 and (b and d) GMI2 (colored curves) compared with NHC best-track data (black curve; 1800 UTC

710 27 Sep to 0500 UTC Oct 2016) for the 120-h forecast started at the analysis time in all 6 analysis-

711 forecast cycles (as listed in the legend). (c) and (d) show mean forecast errors of minimum sea

712 level pressure and maximum surface wind averaged over the forecasts started at the analysis time

713 in all 6 analysis-forecast cycles (6-hourly from 1800 UTC 27 September to 0000 UTC 29

714 September 2016) for CTRL2 (red) and GMI2 (blue). In (e) and (f), the colored numbers on the left

715 and right show the averaged errors over all 6 forecasts in first 60h and 120h HWRF integration,

716 respectively.

717 **Figure 11**: 60-hour mean forecast error of (a) track, (b) minimum sea level pressure, and (c)

718 maximum surface wind averaged over forecasts started from the analysis time of all 7 analysis-

719 forecast cycles for the mature phase of Matthew (6-hourly from 0000 UTC 3 October to 1200 UTC

720 4 October 2016) for CTRL3 (red) and GMI3 (blue).

721 **Figure 12**: Comparison of geopotential height (m) and streamline from (a, d, g) ECMWF-interim

722 reanalysis and (b-c, e-f, and h-i) HWRF forecasts. (b, c) and (e, f) are the HWRF 42-h forecasts

723 valid at 1800 UTC 3 October 2016 at 550 mb and 750 mb, respectively, compared with the

724 corresponding ECMWF-interim reanalysis. (h) and (i) show 60-h HWRF forecasts valid at 1200

725 UTC 4 October 2016 at 800 mb, compared with the corresponding ECMWF-interim reanalysis.

726 The CTRL1 and GMI1 experiments (initiated at 0000 UTC 2 October) are shown in the middle

727 and right panels, respectively.

728 **Figure 13**: Locations and spatial distribution of model profiles and TCI sounding profiles

729 (launched around 1800 UTC 2 October 2015, with distance less than 110 km from the hurricane

730 center). Hurricane centers are shown by dotted circles.

731 **Figure 14**: Vertical profiles of (a, b) root mean square error, and (c, d) mean bias (solid colored

732 lines) and standard deviation (shading) of specific humidity and temperature forecasts and root

733 mean square errors of (e) radial and (f) tangential wind forecasts (initiated at 0600 UTC 2 October

734 and 1200 UTC 2 October 2015) for CTRL1 (red) and GMI1 (blue). Each of the forecasts is verified

735 against TCI soundings launched within a 150-km radius of the hurricane center around 1800 UTC

736 2 October and 1800 UTC 3 October 2015, giving a sample size of 156. Similar to (e) and (f), the

737 root mean square errors of (g) radial and (h) tangential wind forecasts are verified against TCI

738 soundings launched between 150 km and 600 km from hurricane centers, giving a sample size of

739 114.

740 **Figure 15**: Comparison of 30-h temperature (K) forecasts at 650 mb, valid at 1800 UTC 29

741 September 2016, for (b) CTRL2 and (c) GMI2 against (a) GFS analysis at the corresponding time.

742 Hurricane centers are indicated by the crossed circles. Red circles indicate the locations of the

743 large pool of cold air to the east of storm.

744 **Figure 16**: Root mean square error for 30-h forecasts of (a) temperature and (b) specific humidity,

745 verified against GFS analysis. Statistics are averaged over forecasts started from the analysis time

746 of all 6 analysis-forecast cycles (6-hourly from 1800 UTC 27 September to 0000 UTC 29

747 September 2016 during the genesis phase of Matthew) within a 600-km radius of the hurricane

748 centers (blue: CTRL2 and Base; red: GMI2 and Base+GMI).

749 **Figure 17**: Averaged 500- to 850-mb RMSE of specific humidity at 30-h forecast (valid at 0000

750 UTC 29 October 2016). (a) CTRL2, (b) GMI2, (c) Base, and (d) Base+GMI. RMSE is calculated

751 based on forecasts verified against GFS analyses at the valid time.

752 **Figure 18**: 60-hour mean error of (a) track, (b) minimum sea level pressure, and (c) maximum

753 surface wind, averaged over forecasts started from each analysis time of all 6 analysis-forecast

754 cycles of the genesis phase of Matthew (6-hourly from 1800 UTC 27 September to 0000 UTC 29

755   September 2016), for Base (red) and Base+GMI (blue).

756

757

758   **Tables and Table Captions**

759   **Table 1**. The list of experiment configurations

760   **Table 2**. Prescribed regression coefficients to calculate CLW and GWP for GMI brightness

761   temperature included in GSI Version 3.3 (after Garrett et al. 2010)

762

763

764

Table 1. The list of experiment configurations

766

Exp.	Hurricane Case	Data assimilation (DA) period	DA domains and data	DA cycle in d01 with GMI Overpass	DA cycle in d02 with GMI Overpass
CTRL1	Joaquin (2015) Mature	0600 UTC 01 – 1800 UTC 02 October	d01: Conv. obs., Sat. obs. d02: Conv. obs., Sat. obs. d03: Conv. obs.		
GMI1	Joaquin (2015) Mature	0600 UTC 01 – 1800 UTC 02 October	d01: Conv. obs., Sat. obs., GMI d02: Conv. obs., Sat. obs., GMI d03: Conv. obs.	2015100106 2015100112 2015100118 2015100200 2015100206 2015100218	2015100106 2015100200 2015100206 2015100218
CTRL2	Matthew (2016) Genesis	1800 UTC 27 – 0000 UTC 29 September	d01: Conv. obs., Sat. obs. d02: Conv. obs., Sat. obs. d03: Conv. obs.		
GMI2	Matthew (2016) Genesis	1800 UTC 27 – 0000 UTC 29 September	d01: Conv. obs., Sat. obs., GMI d02: Conv. obs., Sat. obs., GMI d03: Conv. obs.	2016092718 2016092806 2016092812 2016092818 2016092900	2016092718 2016092812 2016092900
CTRL3	Matthew (2016) Mature	0000 UTC 03 – 1200 UTC 04 October	d01: Conv. obs., Sat. obs. d02: Conv. obs., Sat. obs. d03: Conv. obs.		
GMI3	Matthew (2016) Mature	0000 UTC 03 – 1200 UTC 04 October	d01: Conv. obs., Sat. obs., GMI d02: Conv. obs., Sat. obs., GMI d03: Conv. obs.	2016100300 2016100306 2016100312 2016100318 2016100400 2016100406 2016100412	2016100300 2016100306 2016100312 2016100318 2016100412
Base	Matthew (2016) Genesis	1800 UTC 27 – 0000 UTC 29 September	d01: Conv. obs, No Sat. Obs. d02: Conv. obs, No Sat. Obs. d03: Conv. obs.		
Base+GMI	Matthew (2016) Genesis	1800 UTC 27 – 0000 UTC 29 September	d01: Conv. obs., add GMI d02: Conv. obs., add GMI d03: Conv. obs.	2016092718 2016092806 2016092812 2016092818 2016092900	2016092718 2016092812 2016092900

767
768

769
770   **Table 2**. Prescribed regression coefficients to calculate CLW and GWP

771   for GMI brightness temperature included in GSI Version 3.3 (after Garrett et al. 2010)

772

CLW		GWP	
$a_{0,clw}$	-0.61127	$a_{0,gwp}$	-3541.46329
c_1	0.00378	g_1	0.00393
c_2	-0.00149	g_2	0.00088
c_3	0.03438	g_3	0.00063
c_4	0.01670	g_4	-0.00683
c_5	0.00228	g_5	0.00333
c_6	0.03884	g_6	-0.00382
c_7	0.02345	g_7	0.00452
c_{12}	-0.00036	g_{12}	0.04765
c_{13}	0.00044	g_{13}	-0.00491
$\hat{c}_1$	1.95559	$\hat{g}$	11.98897
$\hat{c}_2$	2.15143		

773
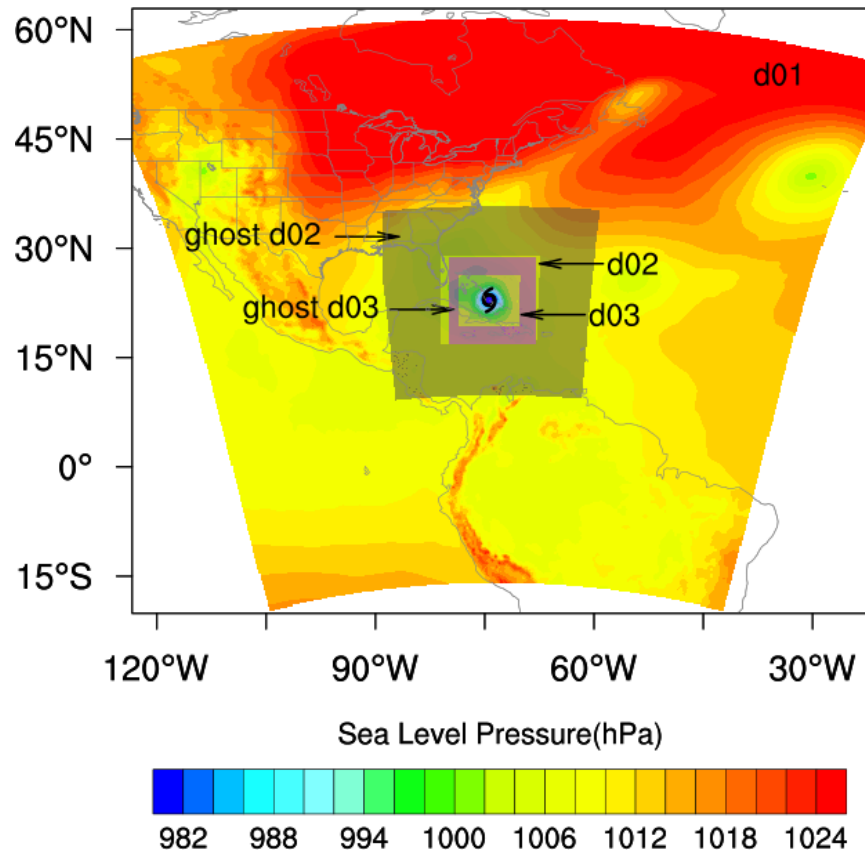
Figure 1. GFS analysis of sea level pressure (color contours, units hPa) and storm center from NHC best track (black storm sign) at 0000 UTC 2 October 2015 for Hurricane Joaquin. HWRF model forecast domains, as indicated by d01, d02, and d03 and HWRF data assimilation domains, as indicated by ghost d02 (black shaded area), and ghost d03 (pink shaded area) are also indicated.

782
783
784   **Figure 2**: Spatial distribution of (a) GMI overpass over ghost d02 at 0000 UTC 2 October 2015,

785   with data that passed QC (colored with O-F values) and failed QC (gray), and (b) GMI

786   observations that failed QC shaded with different colors to denote the type of failure (blue: CLW

787   QC; green: GWP QC; red: emissivity QC). Ghost d02 is shown as an inner domain inside a

788   longitude-latitude box. The hurricane center is indicated by the black cross at the domain center.

789

790
791
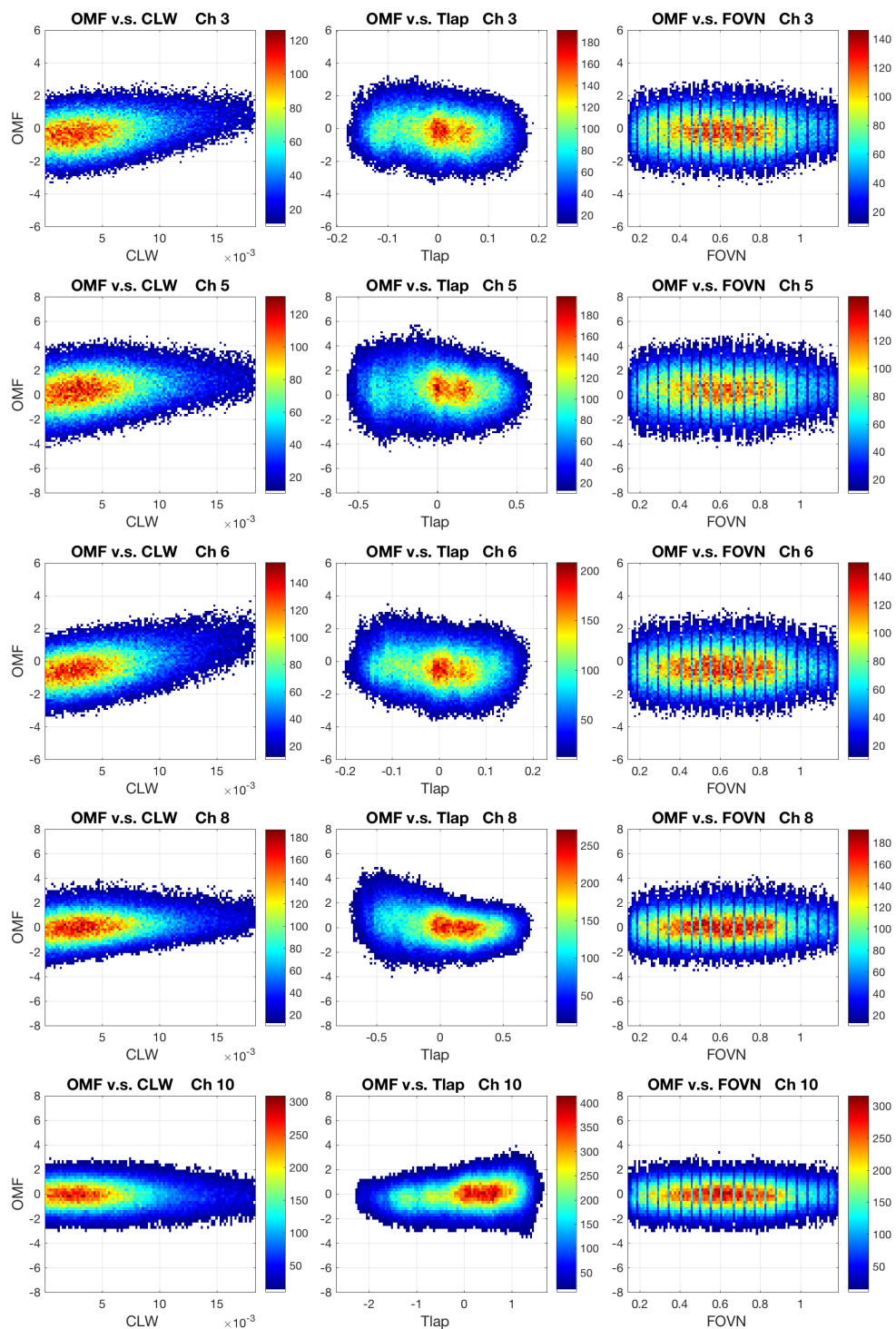
792
793
794 **Figure 3**: Two-dimensional histogram showing the dependence of O-F sample (collected from 26

795 Sep 2015 to 9 Oct 2015) on CLW (left column, (kg/m^2)), Tlap (middle column, (K)) and the field

40

796   of view number (FOVN, right column, (rad)) for Channel 3, 5, 6, 8 and 10. The y-axis denotes O-

797   F value, x-axis represents predictor. The flat distribution around 0 is unbiased.

798
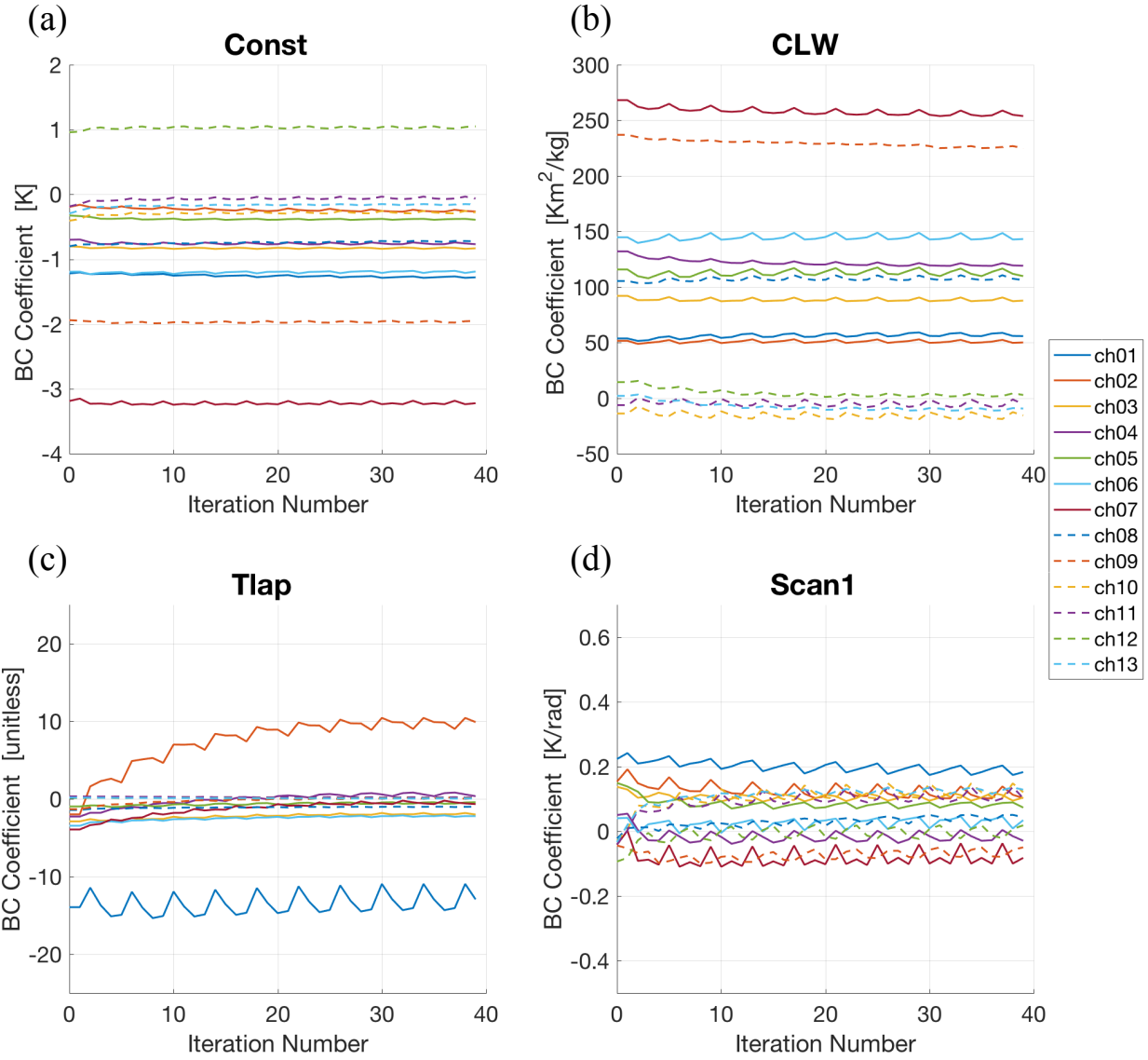
Figure 4: Variation of BC coefficients with the iteration number obtained from Experiment GMI1

for (a) constant offset, (b) CLW predictor (CLW), (c) transmittance lapse rate (Tlap); and (d) Scan

angle.
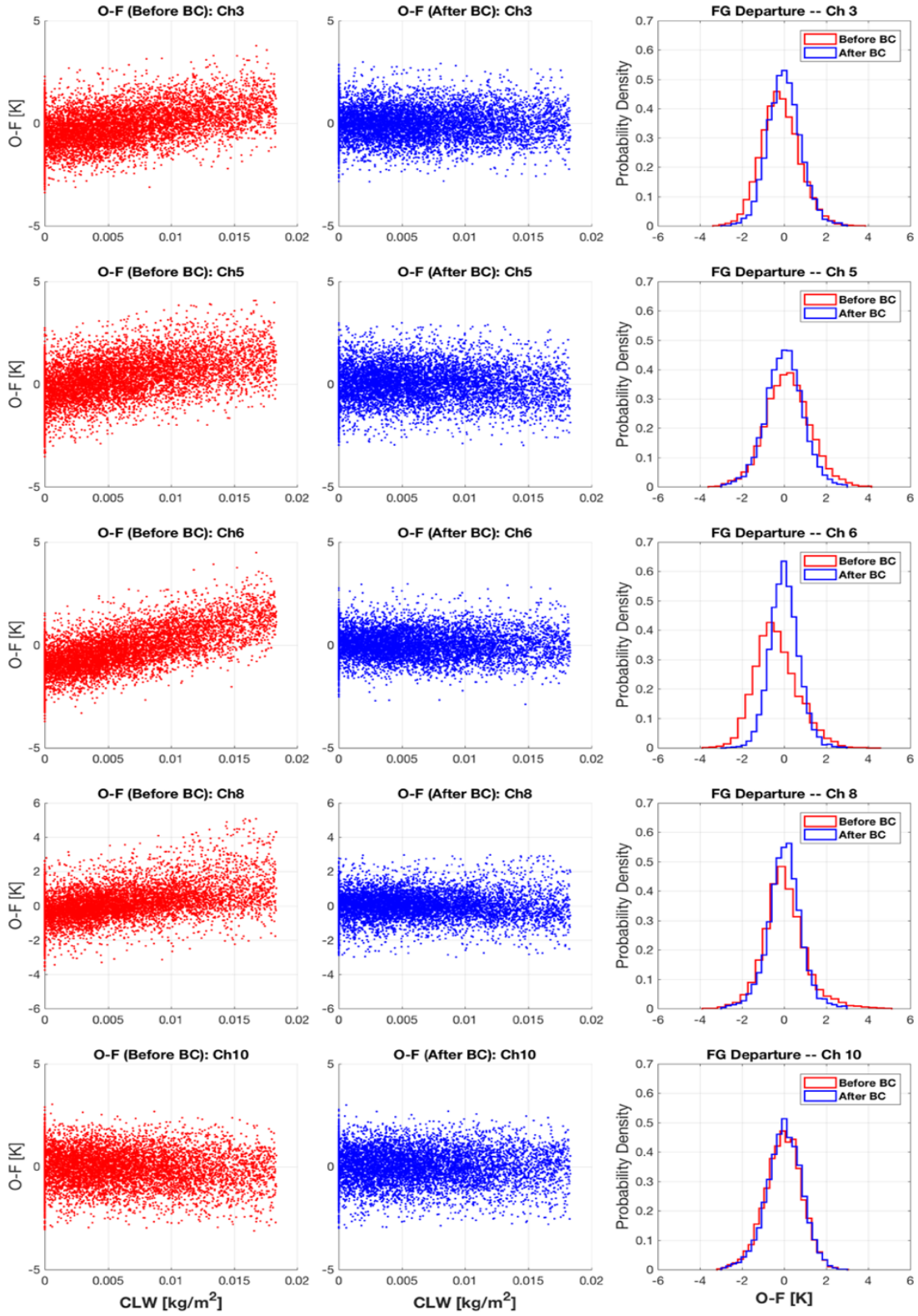
Figure 5: O-F statistics against CLW predictor before (left) and after BC (middle). Histogram of

810   O-F values is shown in the right column. Data sample consists of assimilated GMI observations

811   from 4 analysis-forecast cycles of the mature phase of Joaquin that have major GMI overpasses in

812   the parent domain (0600 UTC 1 October, 1800 UTC 1 October, 0200 UTC 2 October, and 0600

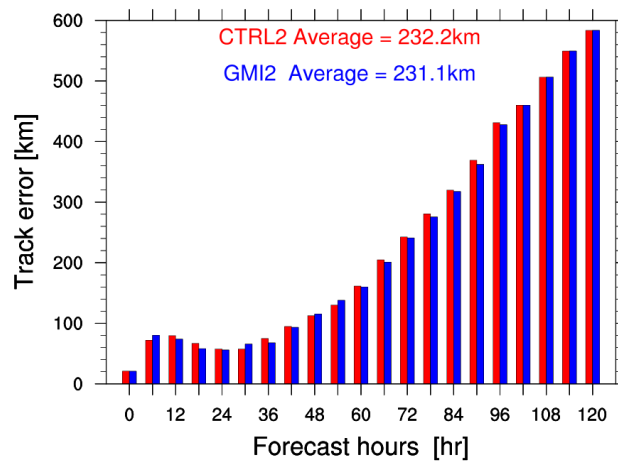813   UTC 2 October 2015).

814
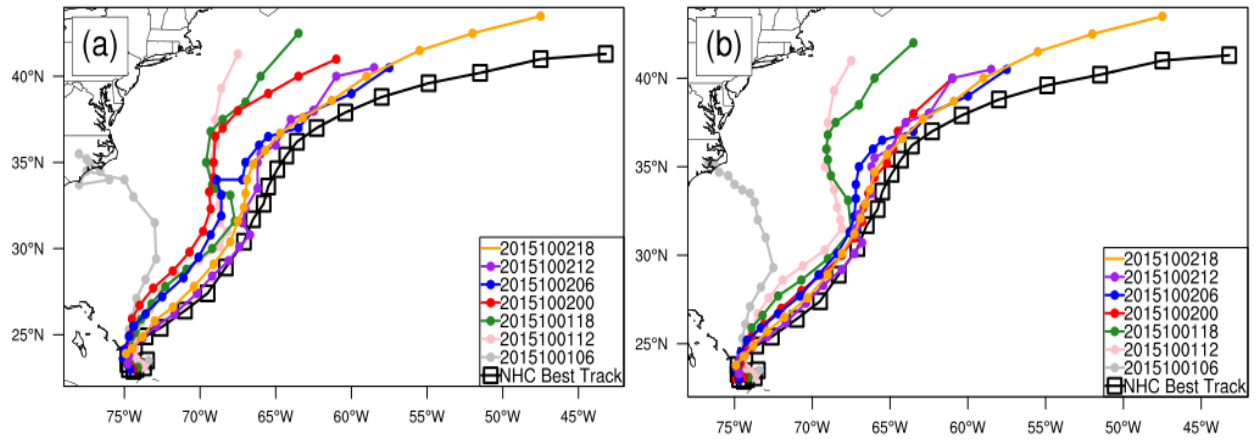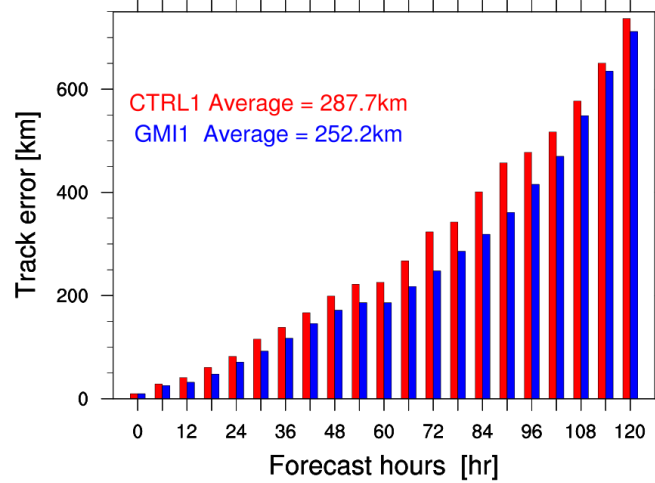
815

816

817

818 **Figure 6**: Comparison of tracks between NHC best track (black curve) with 120-h HWRF

819 forecasts (colored lines) initialed by each of the analyses generated in the 7 analysis-forecast cycles

820 (as listed in the legend) for experiments without and with GMI data assimilation for (a) CTRL1

821 and (b) GMI1. (c) is the 120-h mean track error averaged over the all 7 forecasts in (a) and (b), for

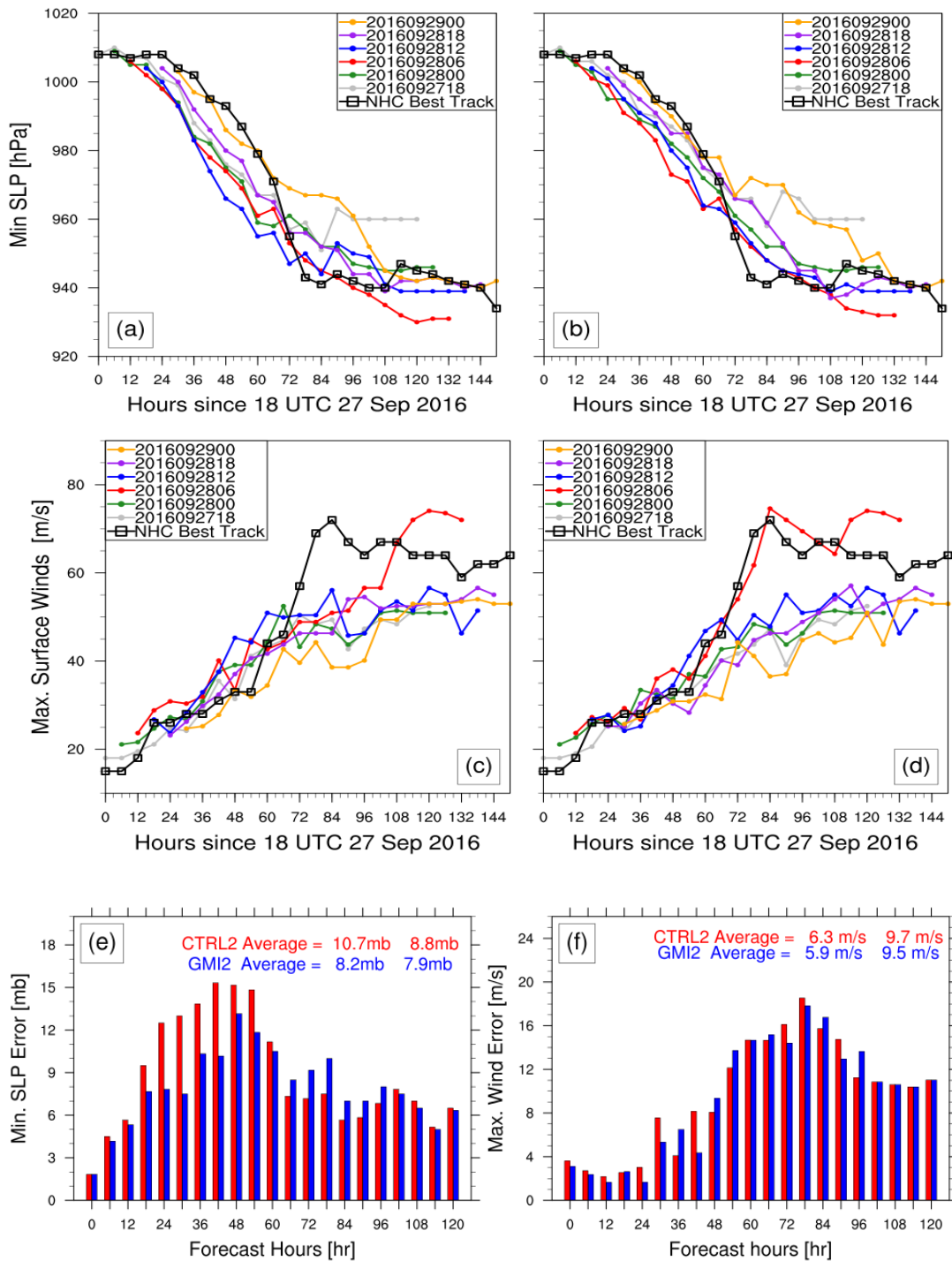822 CTRL1 (red) and GMI1 (blue).

823

824

825

826
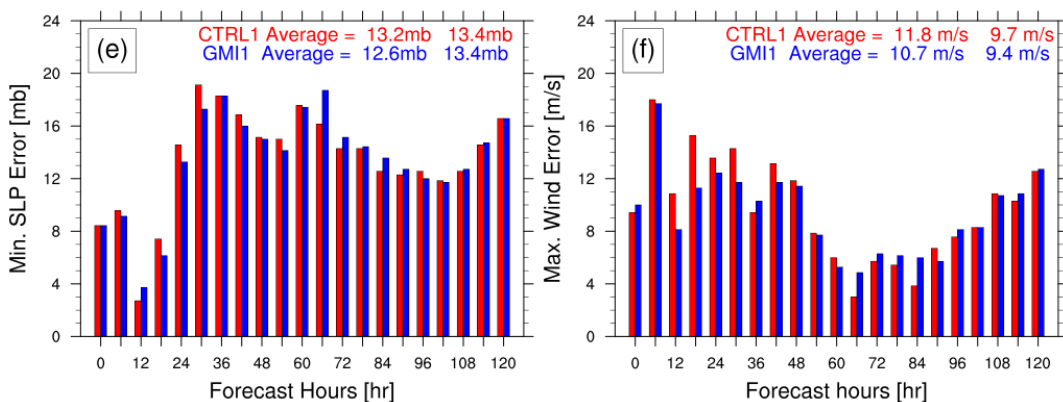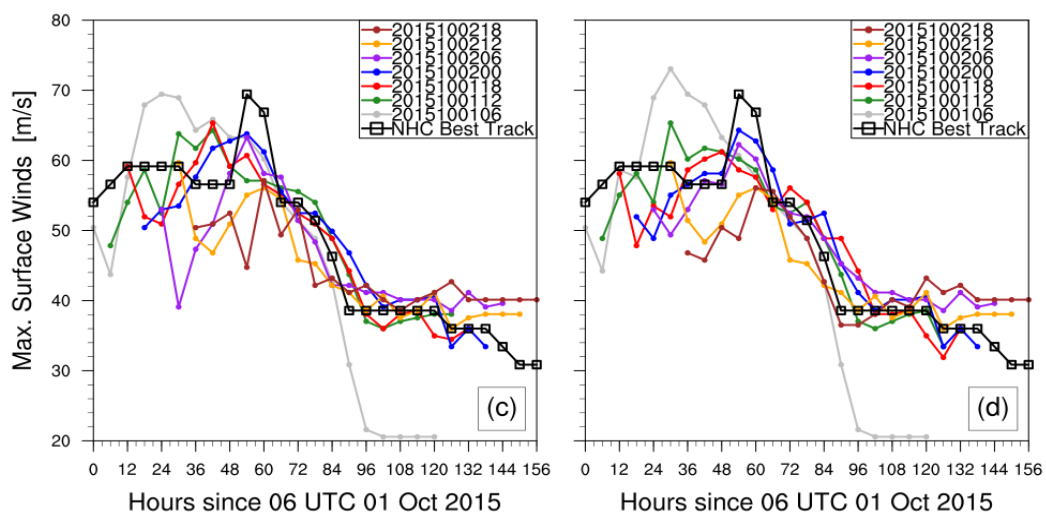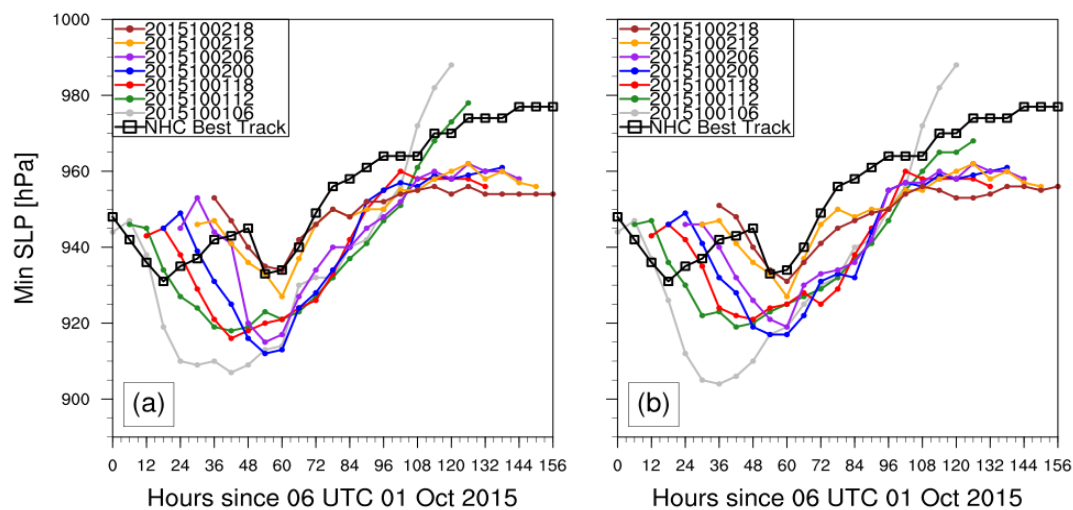
827   **Figure 7**: Aggregated minimum SLP and maximum surface wind forecasts of (a and c) CTRL1

828   and (b and d) GMI1 (colored curves) compared with NHC best-track data (black curve; 06 UTC

829   UTC 01 Oct to 1800 UTC 07 Oct 2015) for the 120-h forecast started at the analysis time in all 7

830   analysis-forecast cycles (as listed in the legend). (e) and (f) show mean forecast errors of minimum

831   sea level pressure and maximum surface wind averaged over the forecasts started at the analysis

832   time in all 6 analysis-forecast cycles (6-hourly from 06 UTC 01 Oct to 18 UTC 02 Oct 2015) for

833   CTRL1 (red) and GMI1 (blue). In (e) and (f), the colored numbers on the left and right show the

834   averaged errors over all 7 forecasts in first 60h and 120h HWRF integration, respectively.

835
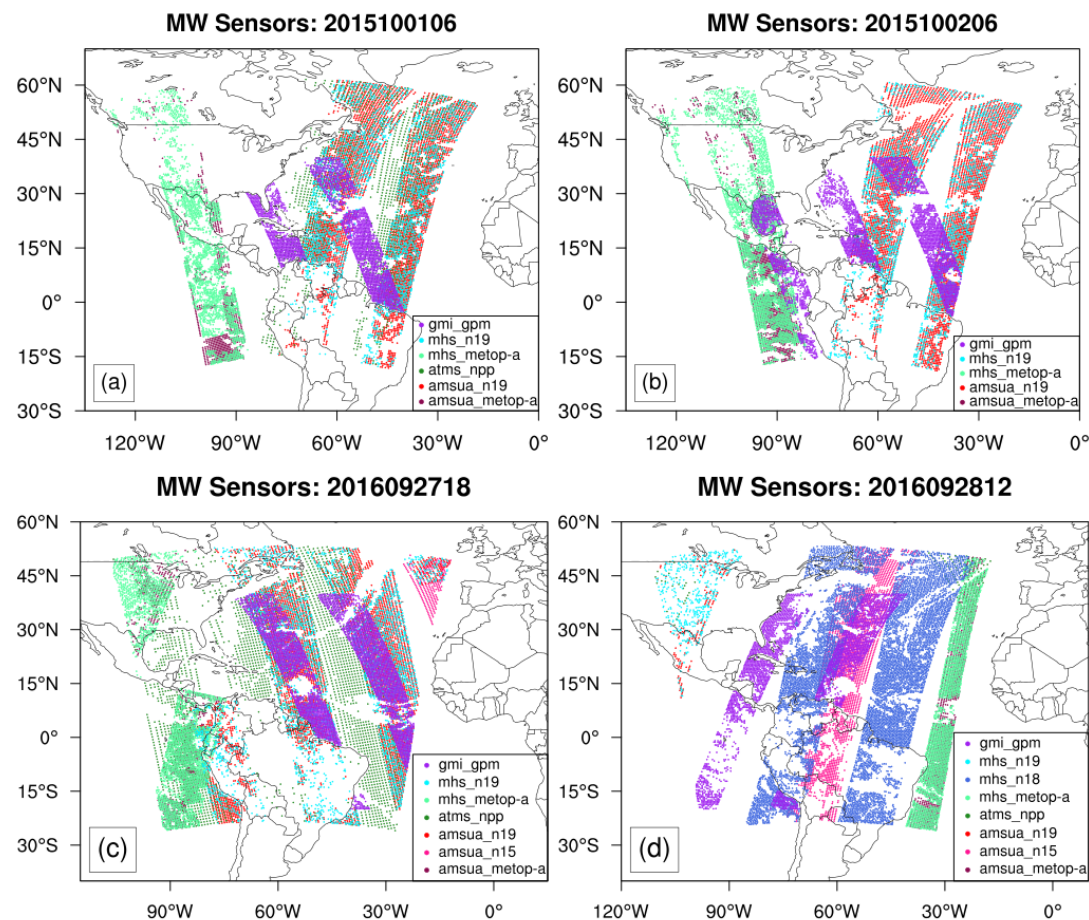
836

837
838
839 **Figure 8**: Assimilated brightness temperature observations of all microwave sensors during the

840 mature phase of Joaquin at (a) 0600 UTC 1 October and (b) 0600 UTC 2 October 2015, and during

841 analysis cycles of the mature phase of Matthew at (c) 1800 UTC 27 September and (d) 1200 UTC

842 28 September 2016. GMI overpasses are highlighted in purple.
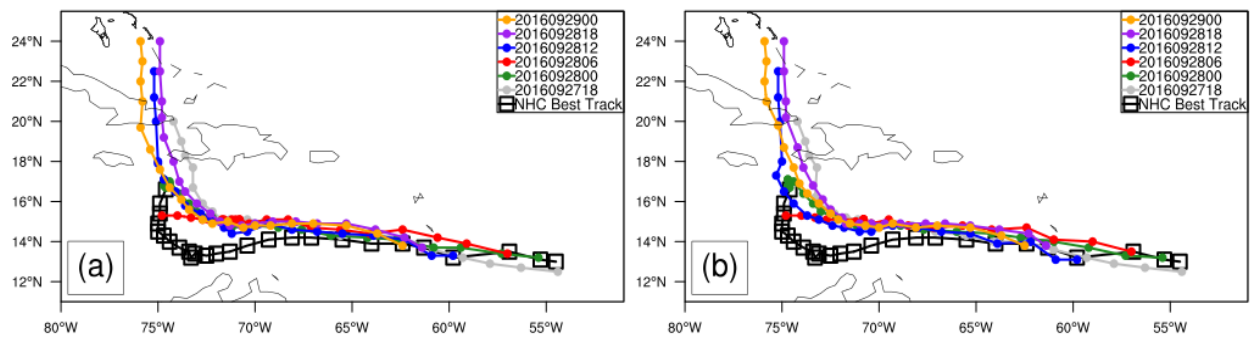
843

844
845

846

847
848
849 **Figure 9**: Comparison of tracks between NHC best track (black curve) with 120-h HWRF

850 forecasts (colored lines) initialed by each of the analyses generated in the 6 analysis-forecast cycles

851 (as listed in the legend) for experiments without and with GM2 data assimilation for (a) CTRL2

852 and (b) GMI2. (c) is the 120-h mean track error averaged over the all 6 forecasts in (a) and (b), for

853 CTRL2 (red) and GMI2 (blue).

854

855
856

857

858
859

860
861

Figure 10: Aggregated minimum SLP and maximum surface wind forecasts of (a and c) CTRL2

and (b and d) GMI2 (colored curves) compared with NHC best-track data (black curve; 1800 UTC

864   27 Sep to 0500 UTC Oct 2016) for the 120-h forecast started at the analysis time in all 6 analysis-

865   forecast cycles (as listed in the legend). (c) and (d) show mean forecast errors of minimum sea

866   level pressure and maximum surface wind averaged over the forecasts started at the analysis time

867   in all 6 analysis-forecast cycles (6-hourly from 1800 UTC 27 September to 0000 UTC 29

868   September 2016) for CTRL2 (red) and GMI2 (blue). In (e) and (f), the colored numbers on the left

869   and right show the averaged errors over all 6 forecasts in first 60h and 120h HWRF integration,

870   respectively.

871

872
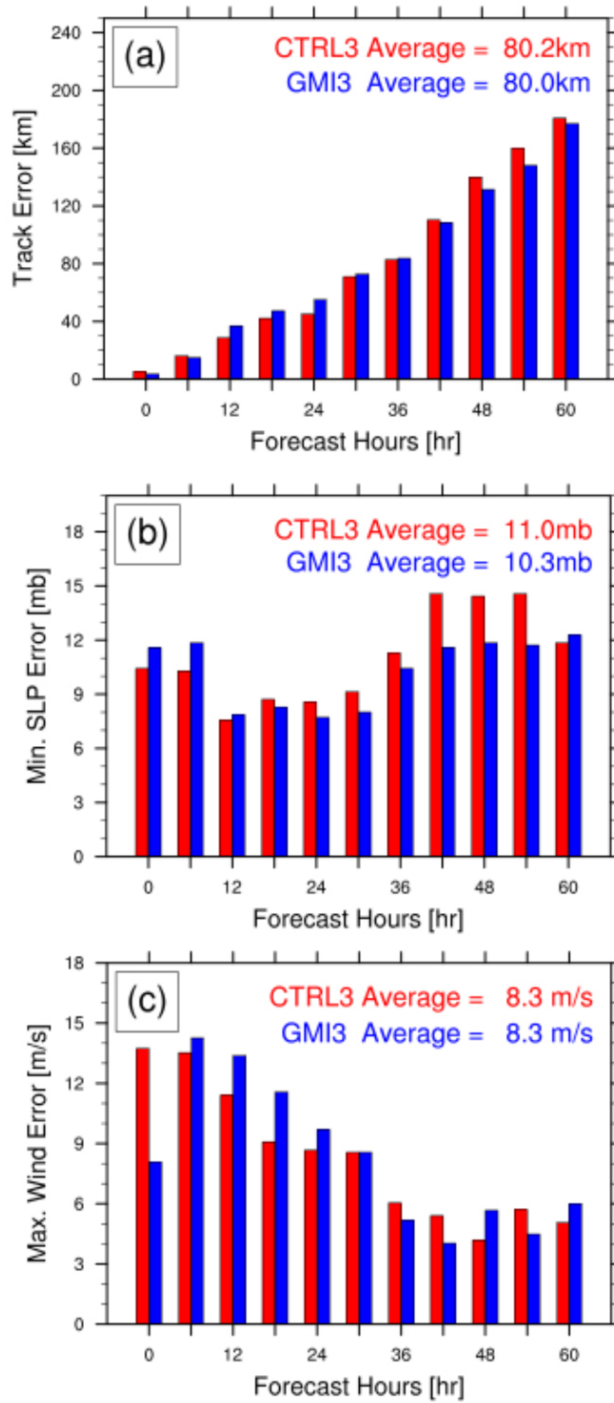
873
874 **Figure 11**: 60-hour mean forecast error of (a) track, (b) minimum sea level pressure, and (c)

875 maximum surface wind averaged over forecasts started from the analysis time of all 7 analysis-

876 forecast cycles for the mature phase of Matthew (6-hourly from 0000 UTC 3 October to 1200 UTC

877 4 October 2016) for CTRL3 (red) and GMI3 (blue).
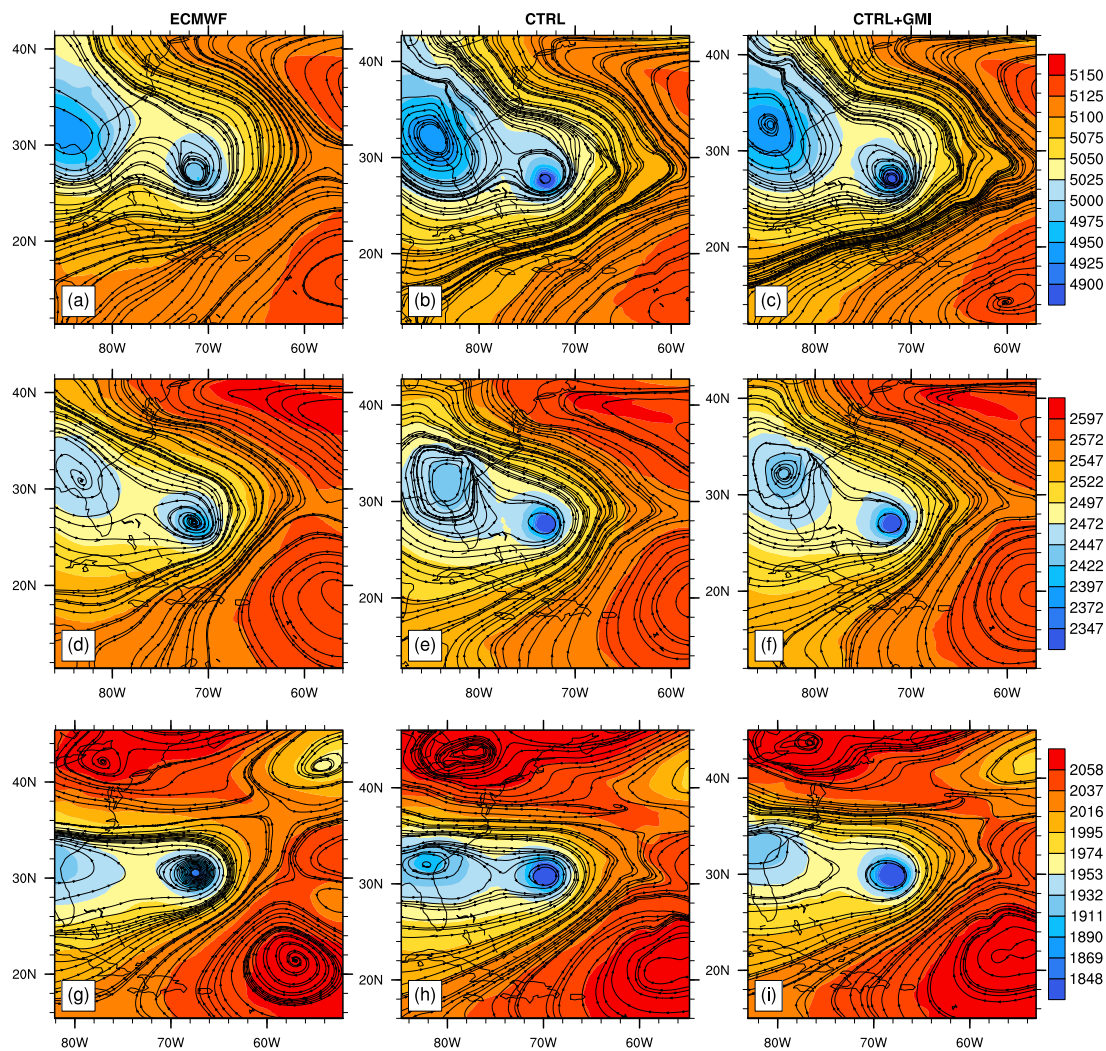
Figure 12:   Comparison of geopotential height (m) and streamline from (a, d, g) ECMWF-interim reanalysis and (b-c, e-f, and h-i) HWRF forecasts. (b, c) and (e, f) are the HWRF 42-h forecasts valid at 1800 UTC 3 October 2016 at 550 mb and 750 mb, respectively, compared with the corresponding ECMWF-interim reanalysis. (h) and (i) show 60-h HWRF forecasts valid at 1200 UTC 4 October 2016 at 800 mb, compared with the corresponding ECMWF-interim reanalysis. The CTRL1 and GMI1 experiments (initiated at 0000 UTC 2 October) are shown in the middle and right panels, respectively.

890

Dropsonde and Model grid location
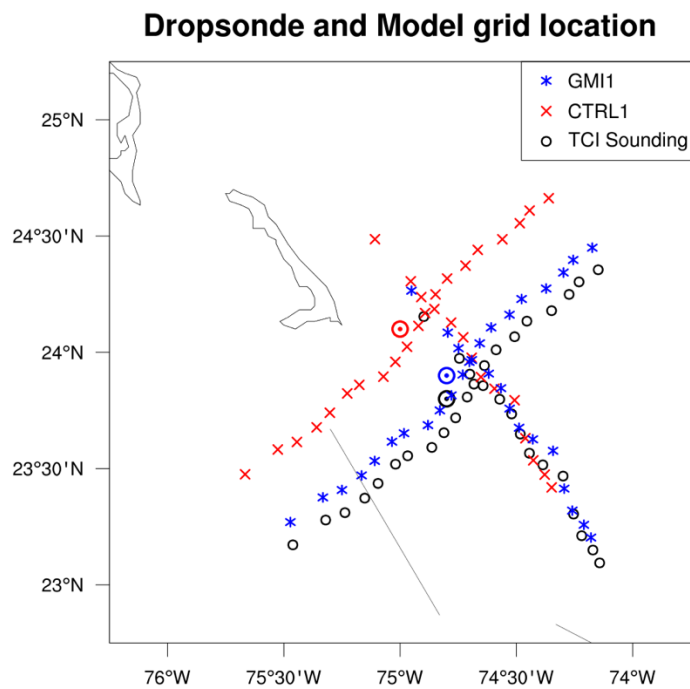
891
892
893   **Figure 13**: Locations and spatial distribution of model profiles and TCI sounding profiles

894   (launched around 1800 UTC 2 October 2015, with distance less than 110 km from the hurricane

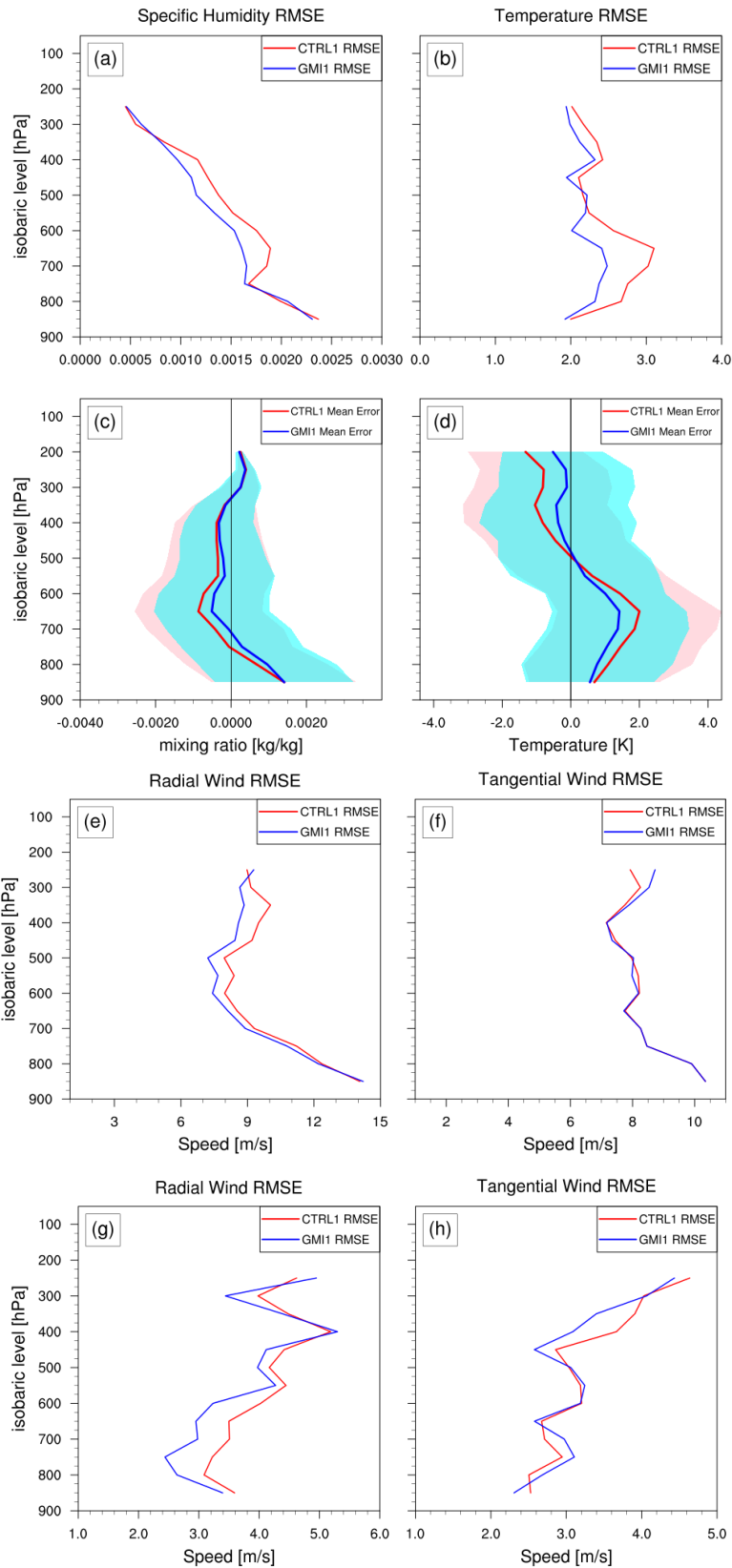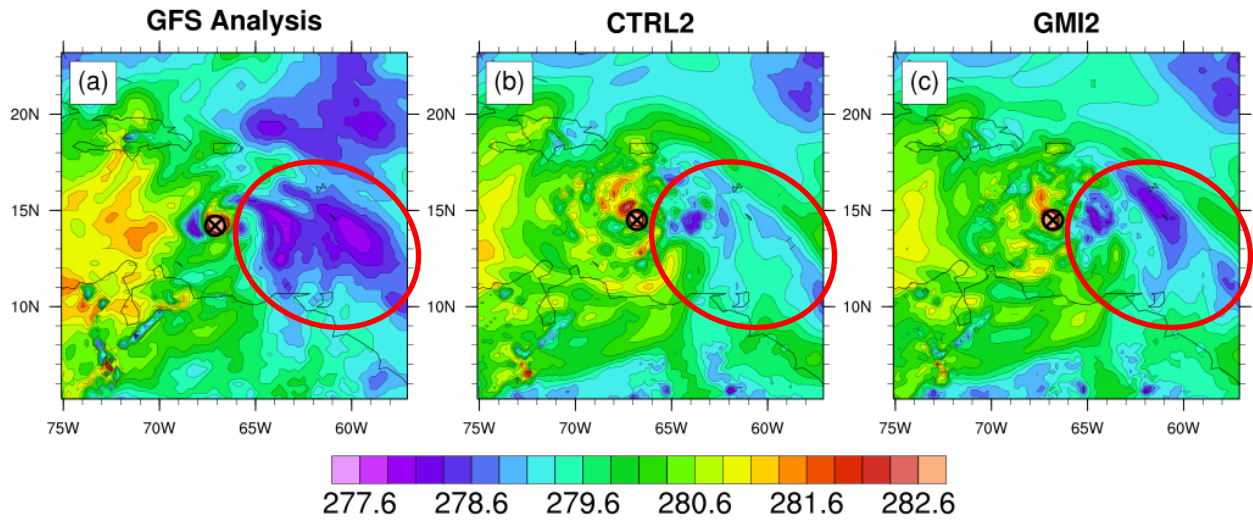895   center). Hurricane centers are shown by dotted circles.

896

897

898
899

900 **Figure 14**: Vertical profiles of (a, b) root mean square error, and (c, d) mean bias (solid colored

901 lines) and standard deviation (shading) of specific humidity and temperature forecasts and root

902 mean square errors of (e) radial and (f) tangential wind forecasts (initiated at 0600 UTC 2 October

903 and 1200 UTC 2 October 2015) for CTRL1 (red) and GMI1 (blue). Each of the forecasts is verified

904 against TCI soundings launched within a 150-km radius of the hurricane center around 1800 UTC

905 2 October and 1800 UTC 3 October 2015, giving a sample size of 156. Similar to (e) and (f), the

906 root mean square errors of (g) radial and (h) tangential wind forecasts are verified against TCI

907 soundings launched between 150 km and 600 km from hurricane centers, giving a sample size of

908 114.

909

910

911
912

Figure 15: Comparison of 30-h temperature (K) forecasts at 650 mb, valid at 1800 UTC 29

September 2016, for (b) CTRL2 and (c) GMI2 against (a) GFS analysis at the corresponding time.

Hurricane centers are indicated by the crossed circles. Red circles indicate the locations of the
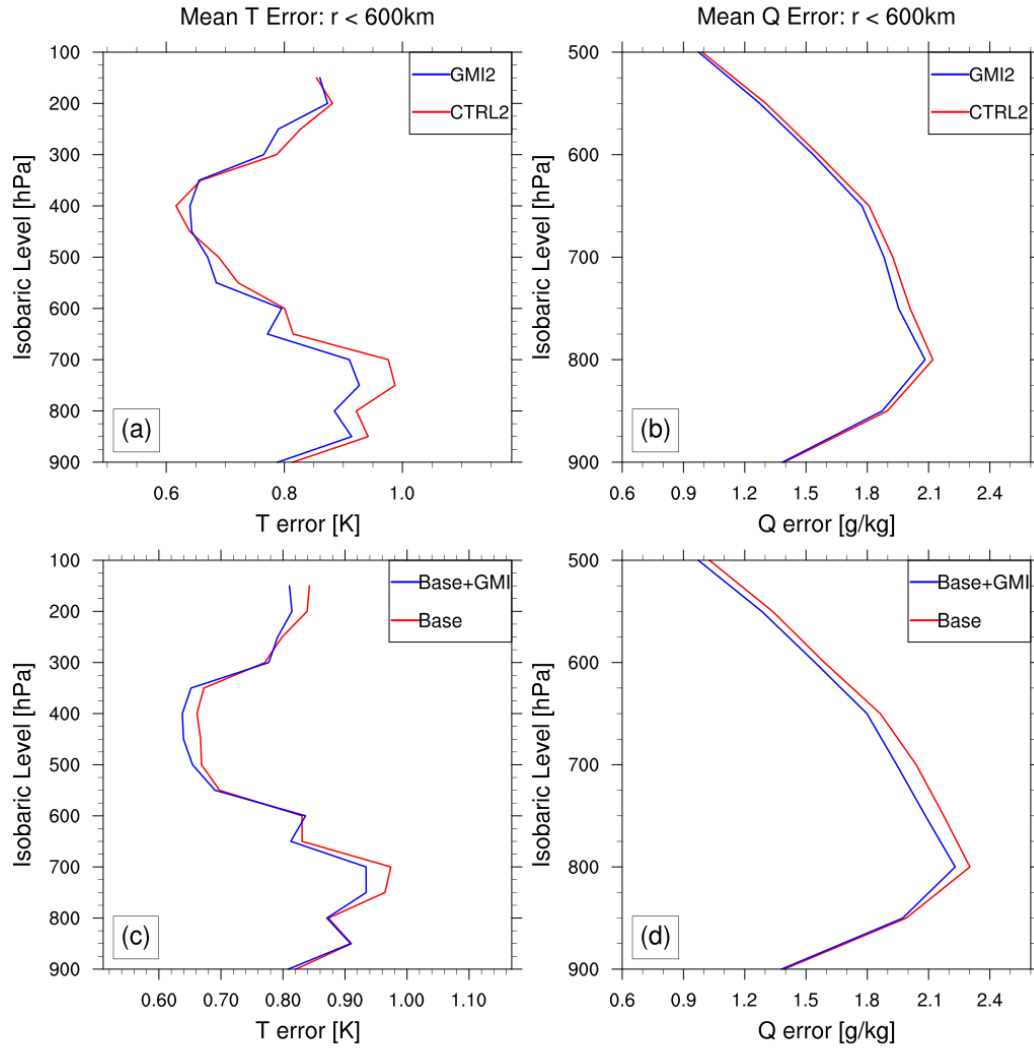
large pool of cold air to the east of storm.

917

Figure 16: Root mean square error for 30-h forecasts of (a) temperature and (b) specific humidity, verified against GFS analysis. Statistics are averaged over forecasts started from the analysis time of all 6 analysis-forecast cycles (6-hourly from 1800 UTC 27 September to 0000 UTC 29 September 2016 during the genesis phase of Matthew) within a 600-km radius of the hurricane centers (blue: CTRL2 and Base; red: GMI2 and Base+GMI).
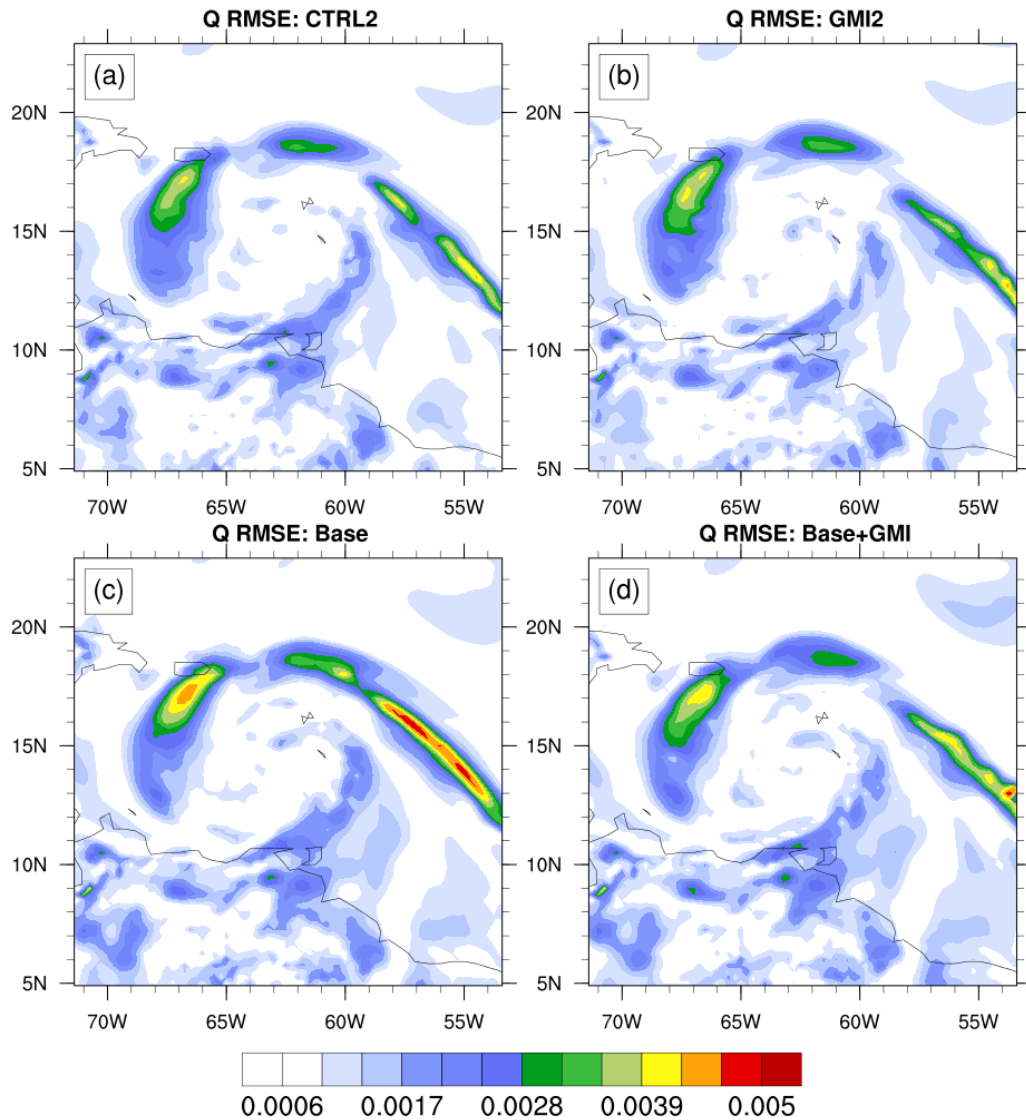
Figure 17: Averaged 500- to 850-mb RMSE of specific humidity at 30-h forecast (valid at 0000 UTC 29 October 2016). (a) CTRL2, (b) GMI2, (c) Base, and (d) Base+GMI. RMSE is calculated based on forecasts verified against GFS analyses at the valid time.
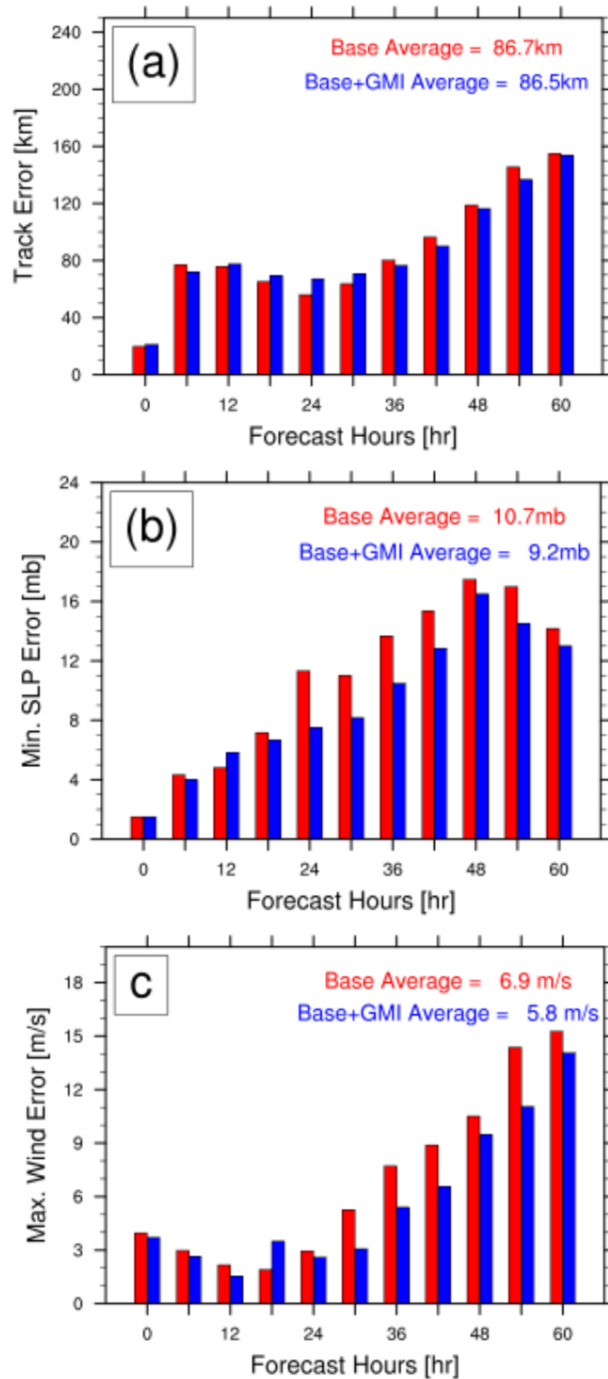
931
932
933   **Figure 18**: 60-hour mean error of (a) track, (b) minimum sea level pressure, and (c) maximum

934   surface wind, averaged over forecasts started from each analysis time of all 6 analysis-forecast

935   cycles of the genesis phase of Matthew (6-hourly from 1800 UTC 27 September to 0000 UTC 29

936   September 2016), for Base (red) and Base+GMI (blue).